



Impact of sedimentology and diagenesis on the petrophysical properties of a tight oolitic carbonate reservoir. The case of the *Oolithe Blanche Formation* (Bathonian, Paris Basin, France)



Yasin Makhloufi ^{a,*}, Pierre-Yves Collin ^b, Françoise Bergerat ^a, Lisa Casteleyn ^c, Steven Claes ^d, Christian David ^c, Beatriz Menendez ^c, Fabrice Monna ^e, Philippe Robion ^c, Jean-Pierre Sizun ^f, Rudy Swennen ^d, Christophe Rigollet ^{g,1}

^a Université Pierre et Marie Curie – Paris 6, UMR CNRS 7193 ISTEP, 4 Place Jussieu, 75252 Paris Cedex 05, France

^b Université de Bourgogne, UMR CNRS 6282 Biogéosciences, 6 Bd Gabriel, 21000 Dijon, France

^c Université de Cergy-Pontoise, Laboratoire Géosciences et Environnement Cergy, 5 mail Gay-Lussac, 95031 Cergy-Pontoise Cedex, France

^d Katholieke Universiteit Leuven, Dept. of Earth and Environmental Sciences, Geology, Celestijnenlaan 200E, 3001 Heverlee, Belgium

^e Université de Bourgogne, UMR CNRS 6298 Culture ARTéHIS, 6 Bd Gabriel, 21000 Dijon, France

^f Université de Franche-Comté, UMR CNRS 6249 Chrono-environnement, 16 route de Gray, 25030 Besançon Cedex, France

^g BRGM, 3 Avenue Claude Guillemin, 45060 Orléans, France

ARTICLE INFO

Article history:

Received 28 February 2013

Received in revised form

19 July 2013

Accepted 19 August 2013

Available online 5 September 2013

Keywords:

Paris Basin

Ooids

Tight carbonate reservoir

Diagenesis

Petrophysics

Porosity

Permeability

Fluid-flow properties

ABSTRACT

The *Oolithe Blanche Formation* was studied in three quarries, located at the south-eastern edge of the Paris Basin (France). Heterogeneities in reservoir properties were assessed through a sedimentological, diagenetic and petrophysical study. The relationships between depositional settings, diagenesis and petrophysical properties were analysed using detailed petrographic studies, image analysis, Nano CT-scans and petrophysical measurements.

The carbonate reservoir pore network is mainly controlled by intraparticle microporosity which ensures the connectivity with interparticle meso- and macroporosity.

Early cementation vs. early compaction processes (mainly grain interpenetration) may have considerable influence on fluid-flow properties and parameters such as permeability, acoustic velocities and tortuosity. Better reservoir properties are found when compaction processes begin before cementation.

From statistical analyses, e.g. Principal Component Analysis and Linear Discriminant Analysis, a sedimentological/diagenetic and petrophysical model is proposed that is in a good agreement with the geological model developed from field work.

© 2013 Elsevier Ltd. All rights reserved.

1. Introduction

In a world where demand for fossil and renewable energy continues to rise, reservoir characterisation and modelling is an essential step for better management of resources. About 60% of the oil and 40% of the gas reserves are present in carbonate reservoirs (Schlumberger Market Analysis, 2007). In this context, such

reservoirs represent a challenge as they are by far the most complex lithologies to understand. Three major difficulties are inherent in the interpretation of carbonate reservoirs: (1) the heterogeneity of reservoir properties in carbonate rocks (e.g. Westphal et al., 2004; Davis et al., 2006; Dou et al., 2011), (2) their often fractured non-matrix flow network and (3) the complex long-term diagenetic evolution of the reservoir (Rong et al., 2012; Wilson and Evans, 2002). It is therefore generally difficult to understand and even more difficult to predict the distribution of petrophysical properties in carbonate reservoirs.

The *Oolithe Blanche Formation* is one of the two major deep saline aquifers in the Paris Basin (France). This formation has been widely used for over thirty years in the exploitation of geothermal energy, especially in the centre of the basin. Furthermore, this reservoir was selected by the French Geological Survey (BRGM) as a

* Corresponding author. Present address: Université Pierre et Marie Curie, ISTEP, 4 Place Jussieu Case 117, 75252 Paris Cedex 5, France. Tel.: +33 144274786; fax: +33 144273831.

E-mail addresses: yasin.makhloufi@upmc.fr, yasin.makhloufi@gmail.com (Y. Makhloufi).

¹ Current address: SGS Horizon Oil, Gas & Chemical Services, Prinses Marietplantsoen, 81, 2595 BR Den Haag, Netherlands.

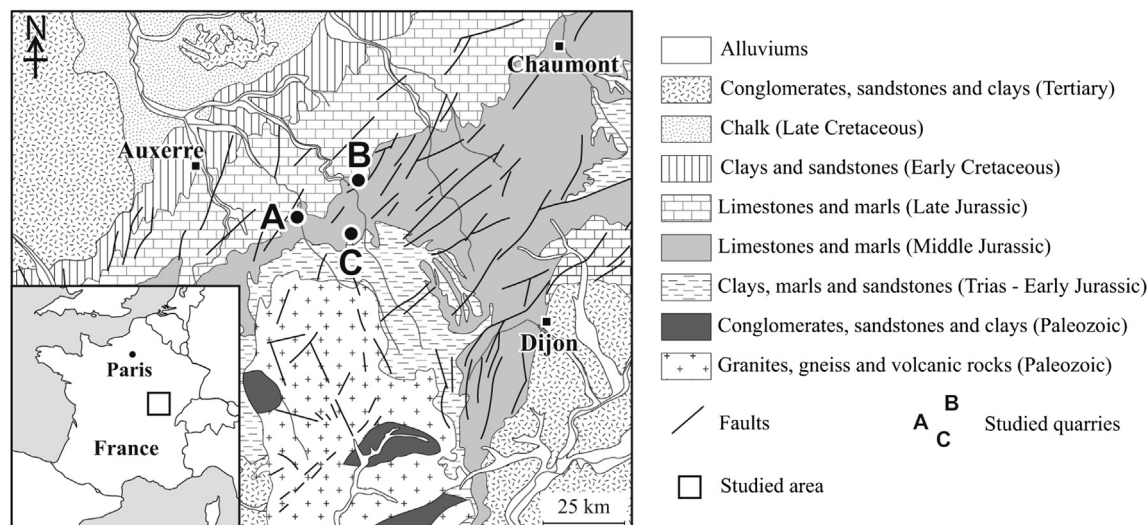


Figure 1. Geological map of the study area and location of sites studied (quarries).

potential target for CO₂ geological storage (Brosse et al., 2010). However, recent studies carried out within the framework of both types of use showed that the petrophysical properties and the distribution of porous and permeable bodies within this aquifer were more complicated than initially expected (Lion et al., 2004; Brigaud et al., 2009, 2010; Delmas et al., 2010; Vincent et al., 2011). In addition, the heterogeneities in the distribution of petrophysical properties are expressed at very different scales, from less than one metre, as observed in outcrops, to more than one kilometre, as shown by geothermal tests (Delmas et al., 2010).

A previous study by Casteleyn et al. (2010a,b) emphasised the fact that the petrophysical properties of the *Oolithe Blanche Formation* are mainly controlled by microstructural properties, and especially by the geometry of the pore network. Based on field analogues, our main objectives are: (1) to provide a detailed diagenetic history of this formation, (2) to complete the data characterising the petrophysical properties of this formation (V_p , permeability and porosity values, pore-throat size, tortuosity, formation factor and 3D reconstruction of the pore network), (3) to define the relationships between petrophysical properties and sedimentological and diagenetic parameters, and finally (4) to propose a model to allow our results to be used in subsurface settings.

A better understanding of porosity and permeability distribution within the facies of the *Oolithe Blanche Formation* will greatly help reservoir modelling, a crucial step for further exploitation of this reservoir. The strategy presented here will help to understand the distribution of reservoir heterogeneities in an uncommon, tight reservoir, with a dominant intraparticle micropore network.

2. Geological setting

The Paris Basin is an intensively studied Meso-Cenozoic intracratonic basin (e.g. Pomerol, 1978; Mégnien, 1979; Guillocheau et al., 1999). It is bounded by ancient massifs, namely the Ardennes to the north, the Armorican Massif to the west, the Vosges to the east and the Massif Central to the south.

In the south-eastern part of the Paris Basin, a Middle Jurassic carbonate series overlies the *Marne à Ostrea acuminata Formation* with, from the base to the top: (1) the *Oolithe Blanche Formation* (Bathonian), which is composed of grainstone (rarely packstone) carbonate, formed in an agitated shallow platform environment,

(2) the *Calcaire de Comblanchien Formation* (Bathonian, locally a hydrocarbon reservoir) composed mainly of wackestone to mudstone carbonate, formed in a calm, protected lagoon environment and (3) the *Pierre de Dijon-Corton Formation*, the *Pierre de Ladoix Formation* and the *Calcaire à Plantes Formation* (usually grouped under the name *Dalle Nacrée Formation*; Floquet et al., 1989; Callovian, locally a hydrocarbon reservoir) mainly composed of coarse oobioclastic deposits formed in a shallow marine environment. This reservoir system is sealed by the *Marne de Massingy Formation* (Callovian-Oxfordian). This reservoir system is included in a larger petroleum system consisting of the Upper Liassic–Dogger–Neocomian, which produced 50% of the Paris Basin oil in 2000 (Beccaletto et al., 2010). During the Bathonian, several large carbonate platforms, including the *Oolithe Blanche Formation*, were present in a warm, agitated, shallow marine domain (Floquet et al., 1989; Garcia et al., 1996; Gaumet et al., 1996; Dromart et al., 2003). These platforms contained oolitic barriers with coarse sediments and lagoonal areas where fine-grained sediments were deposited. The *Oolithe Blanche Formation* is therefore heterogeneous in terms of sedimentology throughout the Bathonian, with horizontal and vertical variations of facies over short distances. The *Oolithe Blanche Formation* varies from 80 to 100 m in outcrops at the eastern edge of the basin, to about 50 m in the centre of the basin, at a depth of 2000 m.

The *Oolithe Blanche Formation* is an oobioclastic limestone with low fossil content (echinoderms, bivalves, brachiopods, gastropods, bryozoans and foraminifers). Ooids found in the *Oolithe Blanche Formation* show laminations typical of marine ooids formed in an agitated environment.

The analysis presented here concerns the *Oolithe Blanche Formation* in three quarries located in the north of Burgundy (Fig. 1) near the towns of Massangis (N 47°37'19.22" E 3°57'22.49"), Bierry-Les-Belles-Fontaines (N 47°36'42.96" E 4°10'48.78") and Ravières (N 47°43'34.92" E 4°14'21.36").

3. Methods

3.1. Sampling

Sites in each of the three quarries were selected and 16 large oriented blocks of about 20 cubic decimetres were collected at each

Table 1
Summary of the petrophysical methods, formulas and parameters investigated.

Method	Investigated parameters	Formulas		Dimensions	Plug size	Conditions
Porosity	Connected porosity	$\Phi = (Ws - Wd)/(Ws - Wh)$	Φ : porosity value in % Ws: weight of saturated sample (g) Wd: weight of dry sample Wh: hydrostatic weight	%	25 mm	Dry, saturated
Mercury porosity	Pore throat diameter	$Pc = 2*\gamma*\cos(\theta)/r$	Pc: Capillary pressure γ : surface tension coefficient of mercury/air r: the radius of the pore throat θ : contact angle, 130° for mercury ⁽¹⁾	μm	25 mm	Dry
Acoustic wave velocity	P wave velocity	$V = d/t$	V: velocity (km/s) d: plug length t: P wave's travelling time	km/s	25 mm	Dry, saturated
Electric conductivity	Formation factor Cementation factor	$F = R_{\text{sample}}/R_{\text{brine}} = \Phi^{-m}$	F: formation factor R: resistivity ($\Omega\text{ m}$) Φ : porosity value m: cementation factor	S m^{-1}	25 mm	Saturated
	Tortuosity	$\tau = F*\Phi = \Phi^{(1-m)}$	τ : tortuosity F: formation factor Φ : porosity value m: cementation exponent		25 mm	Saturated
Capillarity imbibition test	Capillarity imbibition factor	$dW/S = C_i^* \sqrt{t}$	dW: differential of weight gained (g) S: the surface of the sample (cm^2) C _i : capillary imbibition factor t: time (h)	$\text{g cm}^{-2} \text{ h}^{-1/2}$	40 mm	Dry
Permeability	Permeability	$Q = (K/\eta)*S*(\Delta P/L)$	Q: volumetric flow rate of fluid K: permeability η : nitrogen viscosity S: surface of the section L: length of the sample dP: pressure gradient	mD	40 mm	Dry

site. In each block, three separate cores were drilled along the x, y and z axis, one of which was parallel to the bedding, while the other two were perpendicular to the first one. The diameter of the cores depended on the analytical protocols to be applied. While most of the methods were applied to plugs of 25 mm in diameter and 60 mm in length, the permeability measurements and capillary imbibition kinetics required a plug diameter of 40 mm and a length of 55 mm.

To complete our dataset, 31 thin sections were taken from the plugs used by Casteleyn et al. (2010a,b). Hence the complete dataset consisted of 73 samples.

3.2. Petrography and image analysis

Thin sections, impregnated with epoxy resin dyed by Methylene blue, were used to determine the texture, grain type, bioclast content, granulometry, mineralogy, cement type, and pore-type distribution. Cathodoluminescence and calcite staining (Dickson, 1966) were used to determine the cement mineralogy and the sequence of diagenetic events. Thin-section photographs were assembled to obtain an image of each sample as a whole. These images were analysed with the free image analysis software JMicroVision[®], to quantify cementation and grain interpenetration (area in μm^2), grain size and grain count. The cementation surface is calculated based on a colour threshold for the whole image, as the sparitic cementation always appears in white on the photographs. Intraparticle cements were subsequently separated (manually) from interparticle cements and discarded. JMicroVision[®] was also used to quantify grain distribution. Mean grain size was characterised using the maximum length of the grains. We counted 300 grains in each thin section to define sediment composition. The following groups were considered: ooids, echinoderms and others (pellets, bioclasts and undetermined grains). A scanning electron microscope was used to analyse the pore network and to observe the connectivity of the intraparticle and interparticle pore system.

3.3. Petrophysics

3.3.1. Reservoir properties

Lønøy's classification (Lønøy, 2006) was used to characterise the pore types. Three types of pores were differentiated by their size and origin (intra- or interparticle), namely micro- (pore diameter below 1 μm), meso- (pore diameter from 1 to 10 μm), and macropores (pore diameter exceeding 10 μm). Micropores are the dominant type in the reservoir studied, and are always intraparticle.

This petrophysical study follows the procedures described by Casteleyn et al. (2010a,b). A synthesis of the methods, formulas, plug dimensions and laboratory conditions is presented in Table 1. Several of the petrophysical methods applied were measured on water-saturated samples. In such cases the plugs were first oven-dried at 60 °C for 12 h, and then impregnated with water (or brine for the electric conductivity method) in a desiccator for 12 h at a vacuum of 1 Pa. As the device used to measure permeability and capillary imbibition kinetics only accepts plugs of 40 mm in diameter, one plug per sampling block was used, for a total of 31 measurements.

Water porosity was calculated by measuring the dry and water-saturated weight of the sample, and then its hydrostatic weight (weight measurement of the sample totally immersed in water). Mercury Injection Capillary Pressure was measured using a Micrometrics Autopore IV 9500 in order to determine pore-size distribution (Van Brakel et al., 1981) with Washburn's equation (1921).

Capillary rise tests were used to determine the capillary imbibition factor, which describes the capacity of a rock to absorb water only by capillary flow movement. For this experiment, the samples were first dried in an oven at 60 °C and then placed vertically on a grid in a tray filled with distilled water. The level of distilled water was kept constant throughout the duration of the experiment and a thin layer (2–5 mm) of water provided the

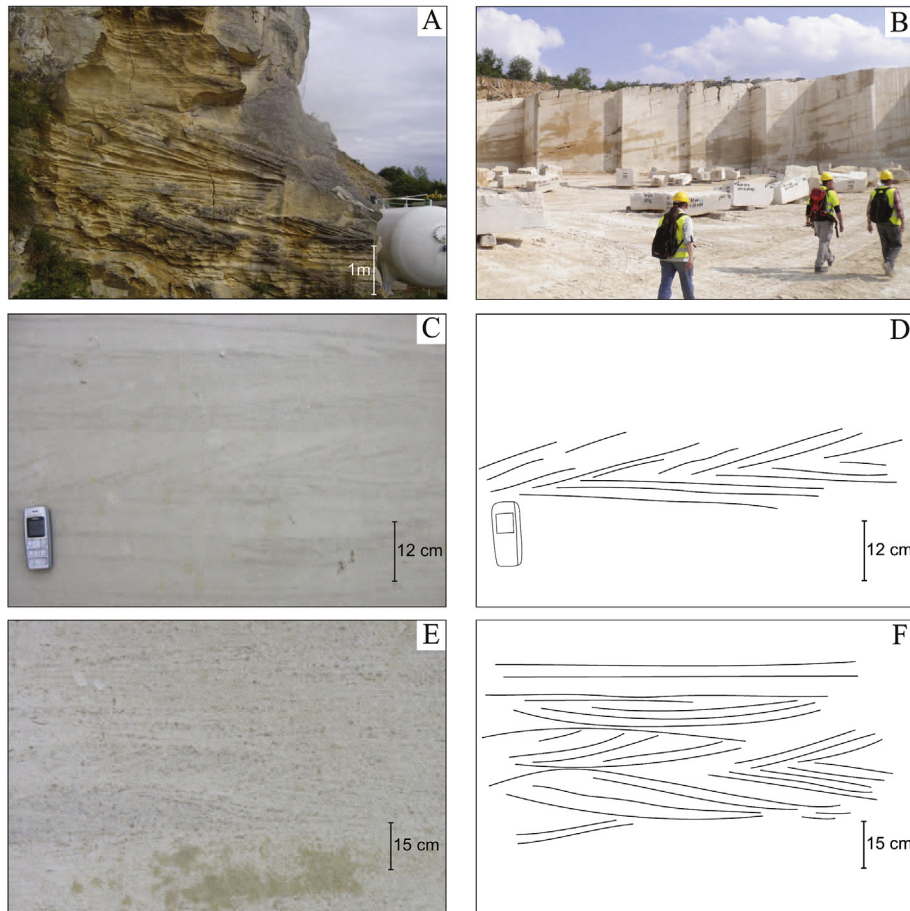


Figure 2. Examples of sedimentary structures observed in the *Oolithe Blanche* Formation. (A) Trough current megaripples and high-energy planar beddings, Oolitic Shoal sub-facies, Ravières quarry. (B) Large structures composed of stacked prograding clinoforms, with lobe morphologies observable when the surface of the structure is visible, Prograding Oolitic Lobe sub-facies, Massangis quarry. (C) Sigmoidal ripples, herringbone cross-stratifications and planar laminations, Tidal sub-facies, Massangis quarry. (D) Outline of sedimentary structures in C. (E). Herringbone cross-stratifications, Tidal sub-facies, Massangis quarry. (F) Outline of sedimentary structures in E.

capillary supply. The tray was sealed and kept at a constant temperature of 25 °C to maintain humidity close to saturation. The weight of the sample was measured at increasing time intervals. The weight increase relative to the surface of the sample was then plotted as a function of the square root of time. The evolution of this weight increase can be separated into two stages. During the first stage the weight gain was linear and the kinematics of imbibition was proportional to the square root of time. The slope of this first stage is the parameter investigated. The second stage of imbibition corresponds to the diffusion in water of the air bubbles trapped in the pore network.

Permeability measurements were performed on a constant head permeameter using nitrogen as fluid. Samples were coated with a neoprene sleeve to maintain a perfect seal in the Hassler chamber during the experiment. Permeability was calculated from Darcy's equation (1856) and corrected for the Klinkenberg effect using the graphical method described by many authors (Riepe et al., 1983; Zinszner and Pellerin, 2007).

3.3.2. Microstructure characterisation

Acoustic velocities were measured using a Panametrics 5058 PR (ultrasonic pulse generator), two ultrasonic P-wave transducers with a resonance frequency of 500 kHz, and a digital oscilloscope. Acoustic P-wave travel time through samples was measured in both dry and saturated conditions, under ambient temperature and atmospheric pressure. Here we present only dry V_p values.

Electric conductimetry tests were performed with a Radiometer CD210 conductimeter in order to determine the formation factor from which the tortuosity and the cementation exponent defined in Archie's law were estimated. This test consists in measuring the electrical conductivity along the axis of a plug saturated with brine (NaCl solution). The saturation process was repeated three times, increasing brine conductivity each time (0.1, 1 and 3 S m⁻¹ respectively). The cementation exponent m was deduced with a regression model based on Archie's law (Archie, 1942). Finally, the electrical tortuosity (Glover, 2009), which represents the complexity of the pore network and the current flow path, was deduced using the relationship between formation factor and porosity (Table 1).

To illustrate the 3D structure of the pore network, computed tomography analyses were carried out, using a GE Measurement & Control Phoenix nanotom[®] with a 180 kV/15 W nanofocus X-ray tube and a tungsten/diamond X-ray source. Achieved resolution ranged from 12 to 1.5 μm/voxel. Plug imaging and pore network connectivity used Avizo[®] Fire 3D analysis software.

3.4. Statistical analysis

A Principal Component Analysis (PCA) was carried out on the measured variables using their correlation matrix (readers can refer to Wold et al. (1987) for a complete description of this method).

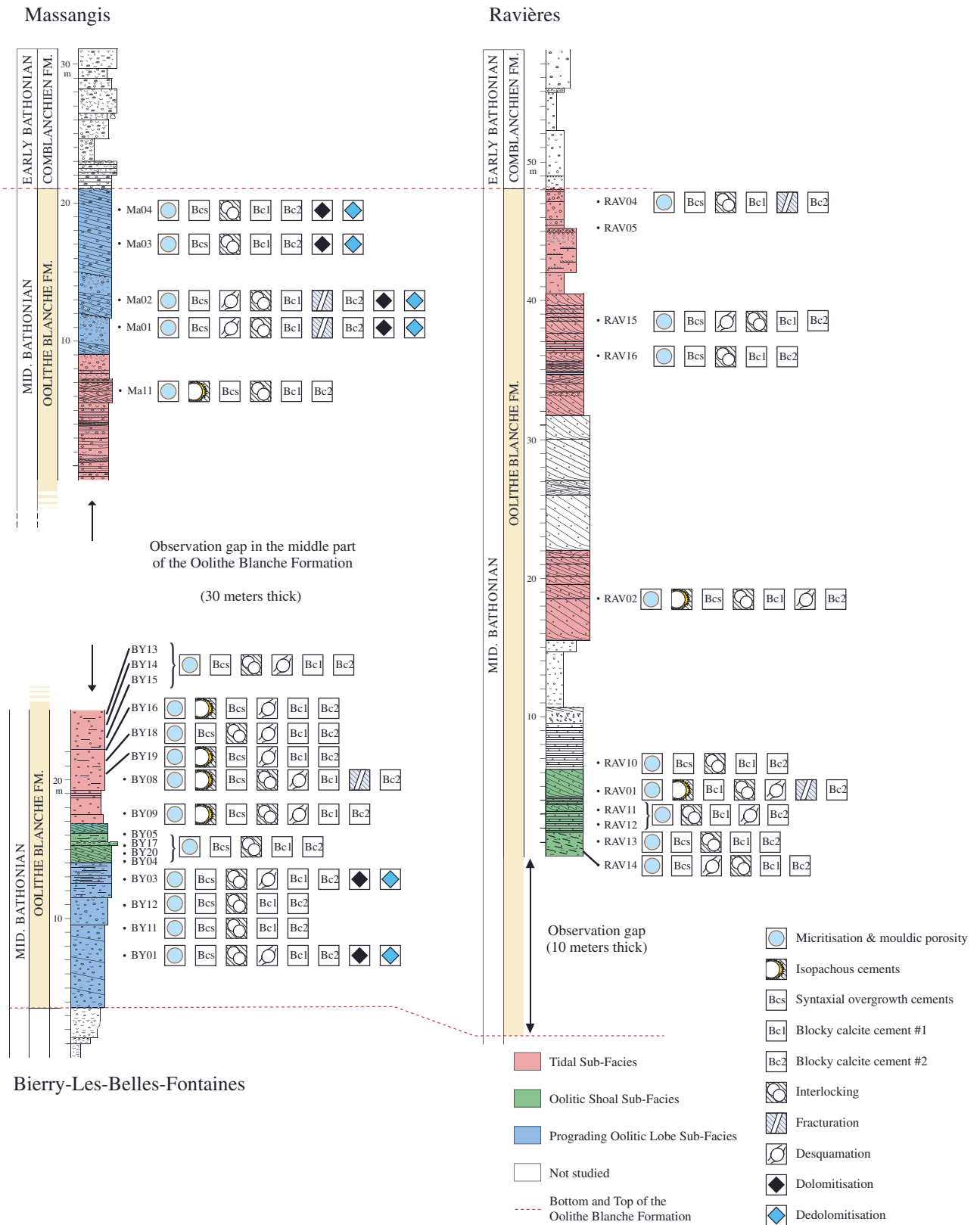


Figure 3. Stratigraphy and logs of the study area. For each sample, the diagenetic phases observed are represented by symbols, from left to right, in chronological order of appearance. Modified from Casteleyn et al. (2010a) (RAV = Ravières, BY = Bierry-Les-Belles-Fontaines, MA = Massangis).

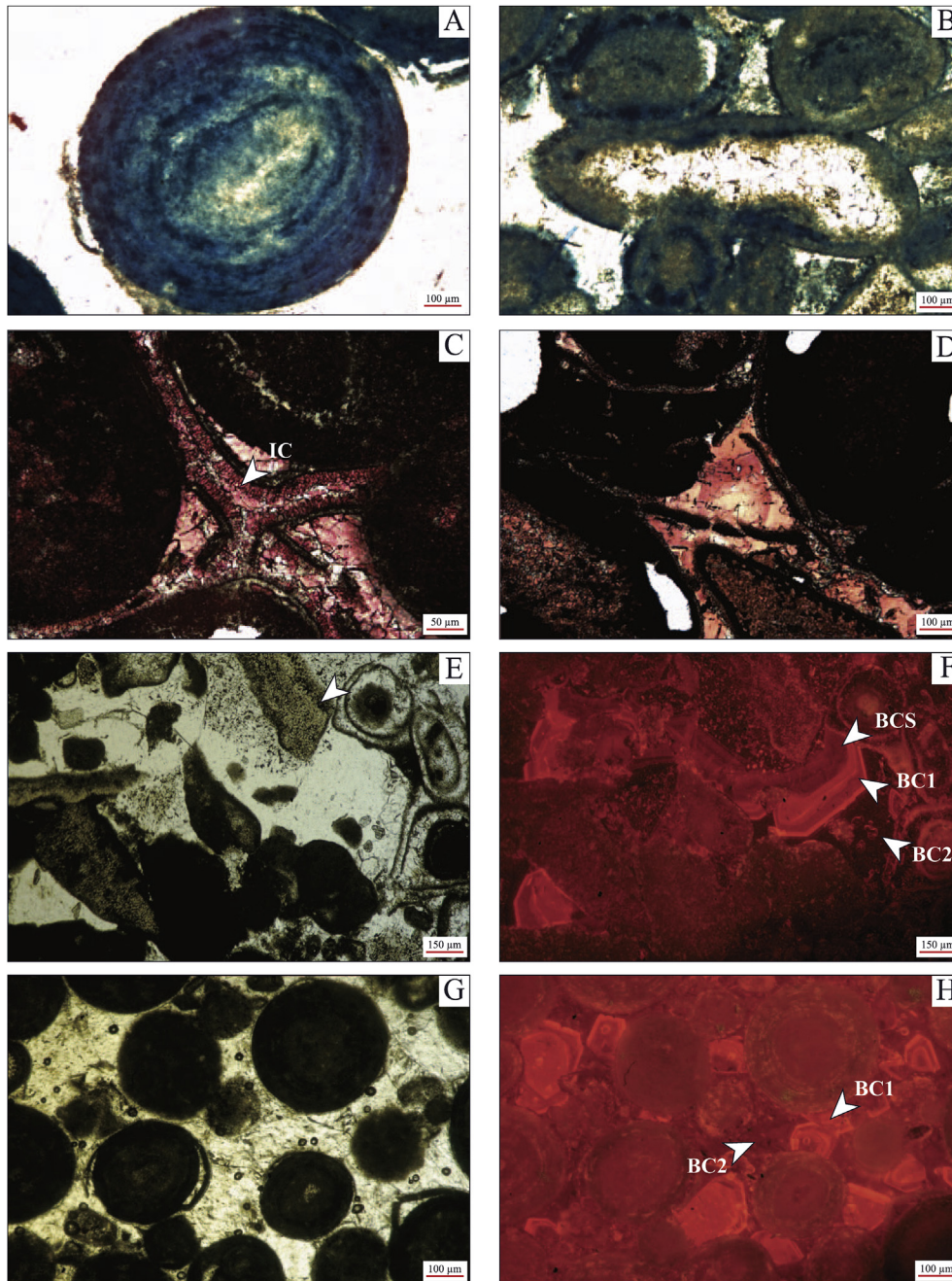


Figure 4. Diagenetic processes, biological and chemical phases. IC: isopachous cement, BCS: syntaxial overgrowth, BC1: blocky calcite #1, BC2: blocky calcite #2. (A) Ooid. The intraparticle micropore system is revealed by a blue-stained resin impregnation. (B) Micritised bioclast observed in polarised non-analysed light under optical microscopy. Mouldic porosity is completely filled with blocky calcite cementation. (C) Isopachous cementation on spalled oolites; the calcite-staining method reveals the low to non-ferroan composition of the cement. (D) Blocky calcite after calcite staining. As with the isopachous cements, the blocky calcite is low to non-ferroan but exhibits zonations. (E) and (F) Syntaxial overgrowth around a non-micritised echinoderm and blocky calcite observed under optical microscopy and cathodoluminescence. (G) and (H) Interparticle blocky calcite filling the primary porosity. Under cathodoluminescence, three cements can be observed, one with ill-defined zonation and brown colouring, corresponding to syntaxial overgrowth (BCS), a second with orange to red zonation (BC1) and a third type with brown colouring, but no zonation (BC2). (For interpretation of the references to colour in this figure legend, the reader is referred to the web version of this article.)

To validate the fact that petrophysical properties are dependent on the facies (and are thus sedimentologically controlled) a Linear Discriminant Analysis (LDA, see [Lachenbruch and Goldstein, 1979](#)) with cross-validation was carried out. The LDA is a predictive method to study the possible relationship between several groups of individuals. In the present work, each individual is characterised by diagenetic and petrophysical measurements. The aim is to determine that an individual belongs to a group of samples sharing

the same properties. The comparison is then made between the groups established by the LDA and the sedimentological groups (i.e. sub-facies) observed in the outcrops. A good match between the LDA and field-work investigations means that the classification is successful. This would strengthen the hypothesis that depositional setting induces particular diagenetic/petrophysical properties. This will also provide a way to predict the facies when only laboratory measurements are available. To ensure the validity of our analysis,

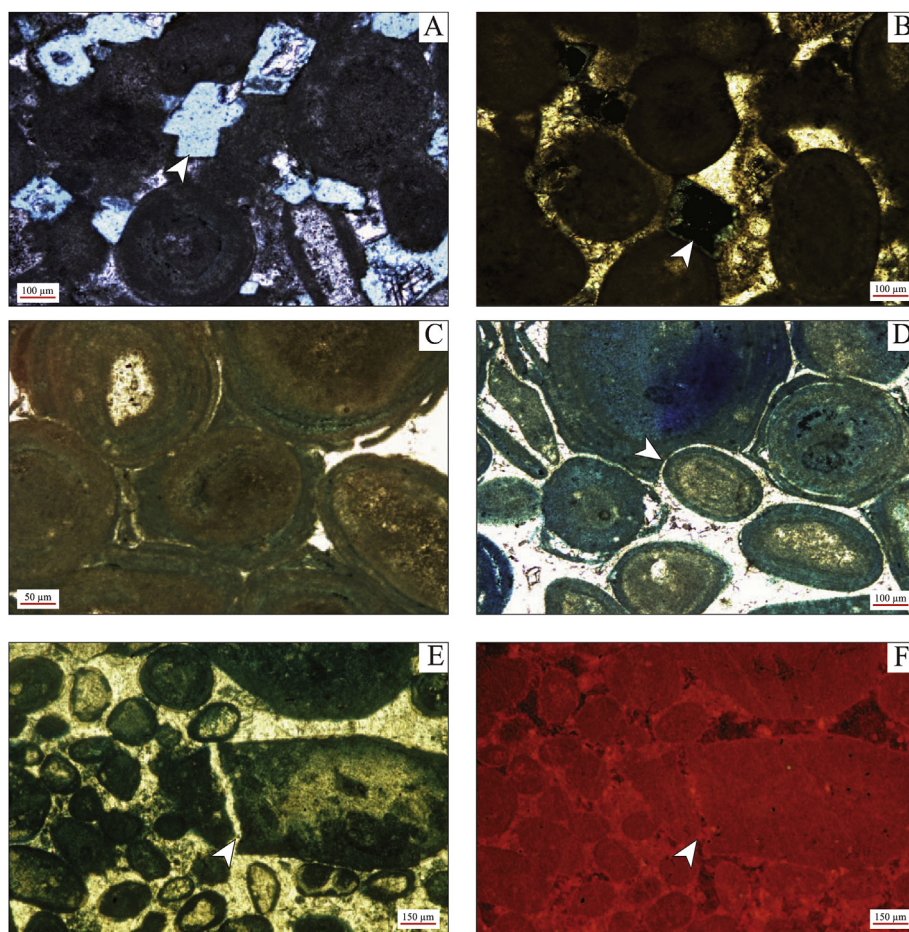


Figure 5. Diagenetic, chemical and physical phases. (A) and (B) Macroporosity showing a rhombohedral morphology, typical of dedolomitisation. This phase truncates the particles as well as the cements. (C) interpenetrated ooids. The intraparticle microporosity is revealed by the impregnation with blue staining. (D) Rare case of isopachous cementation trapped during grain interpenetration. (E) and (F) Micro-fracturing filled with blocky calcite. (For interpretation of the references to colour in this figure legend, the reader is referred to the web version of this article.)

we used the Wilks test (Shapiro and Wilk, 1965). The null hypothesis was that the facies are all identical and cannot be discriminated by the diagenetic and petrophysical parameters considered. Statistical analyses were performed with the free software R (R Core Team, 2012).

4. Results

4.1. Sedimentary facies of the Oolithe Blanche Formation

Three sedimentary sub-facies were recognised in the *Oolithe Blanche Formation*. The term facies is used hereafter for the general facies of the formation (i.e. an oolitic facies), and the term sub-facies for the subdivisions:

- **Oolitic Shoal** sub-facies. These white grainstones are well sorted, and ooids represent 60%–100% of the allochems. The remaining allochems are pellets and various bioclasts (mainly echinoderms (11%), bivalves, brachiopods, corals and benthic foraminifers). In thin sections, an average of 10.4% of the area is occupied by interparticle blocky calcite cementation. Sometimes these grainstones exhibit no sedimentary structures. Planar (2D) or trough (3D) current ripples or megaripples are often observed, as well as coarser horizontal planar laminations (Fig. 2A).
- **Prograding Oolitic Lobe** sub-facies. These white to orange grainstones (or packstones for a few samples) are poorly sorted. Ooids represent 64% of the allochems. Bioclasts are represented by echinoderms (9%), bivalves, brachiopods and benthic foraminifers. A micritic matrix is rarely observed in the samples and is not representative of the main carbonate texture. In the thin sections, an average of 6.3% of the area is occupied by interparticle blocky calcite cementation, the lowest value of the three sub-facies. In the quarries, large structures composed of stacked prograding clinoform sets are observed (Fig. 2B). Planar and trough clinoform sets are recognised. Lobe morphologies can sometimes be observed where the clinoform surfaces are visible. Within the beds, trough cross-stratifications, 3D current ripples and sigmoidal ripples are occasionally present.
- **Sub-facies of tide-dominated environment** (abbreviated as **Tidal** sub-facies). These white grainstones are generally well sorted. Ooids represent 72% of the allochems, with some pellets and bioclasts (mainly echinoderms (11%), bivalves, brachiopods and benthic foraminifers). In the thin sections, an average of 11.6% of the area is occupied by interparticle blocky calcite cementation. Trough cross-beddings, 3D (rarely 2D) ripples and mega-ripples, sigmoidal ripples, herringbone cross-stratifications and horizontal planar laminations are observed (Figs. 2C, D, E and F).

Table 2
Petrophysical and diagenetic variables. Data in italics are compiled from Casteleyn et al. (2010a). Missing values are caused by analytical problems or unavailability of material. G.I.: Grain interpenetration, C.I.F.: Capillary Imbibition Factor.

Sample	Sub-facies	Permeability (mD)	Porosity (%)	Cement (%)	G.I. (%)	VP dry (km/s)	Formation factor	C.I.F. ($\text{g cm}^{-2} \text{h}^{-1/2}$)	Tortuosity	Mean grain size (μm)	
By 12 y	Prograding Oolitic Lobe		19.81	4.27	1.21	3.92	44.19		8.76	404.15	
By 12 z		0.19	17.86	13.69	0.31	4.04	47.44	87.89	8.47	369.53	
Ma 01 z		0.07	15.54	2.31	1.20	4.92	86.27	6.71	11.02	566.52	
Ma 02 x			12.84	2.04	1.42	4.74	71.15	25.03	7.88	572.74	
Ma 02 z		0.03	12.84	3.66	1.20	5.02		22.14	7.88	428.88	
Ma 03 y			12.54	5.28	1.87	4.38	55.11	38.15	7.25	476.16	
Ma 03 z		0.07	13.44	4.70	2.33	4.46	49.58	37.00	7.25	532.85	
Ma 04 x			10.58	1.00	0.23	4.95	88.79	27.29	14.05	452.83	
Ma 04 y			7.75	1.00	0.60	5.67	241.51	24.36	14.05	323.08	
Ma 04 z		0.06	15.71	4.51	1.04	5.08		30.22	14.05	355.34	
By 01 z			8.94	19.25	10.44	0.50	3.66	25.65	118.15		
By 03 z			0.23	16.63	8.73	0.52	3.47	27.87	128.49	4.72	329.54
By 11 x				27.59	6.41	0.53	3.77	23.55		5.05	792.56
By 11 y			19.64	12.39	0.25	3.73	25.52		5.05	389.63	
By 11 z		0.68	19.70	14.01	0.29	3.67	27.82	112.52	5.05	757.52	
By 17 x	Oolitic Shoal		13.11	20.48	0.91	3.49	34.39	61.49	5.63	605.45	
By 17 y		0.42	13.58	14.56	0.76	3.17	51.58		8.58	455.56	
By 17 z			16.89	10.21	1.76	3.23	47.43		8.33	508.12	
By 20 x				18.30	9.37	1.23	3.56	58.31		8.90	451.25
By 20 y		0.29	16.37	12.43	0.30	3.92	57.06	71.61	10.16	374.95	
By 20 z			16.64	10.90	0.76	3.83	21.00		3.88	413.10	
Ra 10 x				17.56	2.81	1.34	3.64	63.06		8.33	319.50
Ra 10 y				16.72	3.62	1.62	3.56	44.39		7.82	394.14
Ra 10 z		0.22	17.05	6.11	1.03	3.71	91.41	82.57	10.09	484.20	
Ra 11 x			15.27	5.11	0.67	3.22	121.62		12.41	302.42	
Ra 11 y			17.80	6.04	0.35	3.41	157.26		18.63	440.86	
Ra 11 z		0.26	18.49	5.72	0.36	3.24	48.71	93.57	7.59	341.11	
Ra 12 x			13.21	8.59	0.18	4.05	47.98		6.01	564.26	
Ra 12 y	0.09	17.62	4.11	0.87	3.59	72.72	52.88	9.51	443.77		
Ra 13 x		11.04	5.34	1.57	3.68	31.25		4.24	415.30		
Ra 13 y		10.21	8.06	0.53	4.22	12.55		2.12	440.40		
Ra 13 z	0.06	11.85	4.55	0.16	3.94	23.89	20.95	4.06	314.00		
Ra 14 x		15.58	11.34	0.97	2.80	46.21		7.14	470.52		
Ra 14 y		12.53	6.17	2.12	3.61	24.66		5.31	806.60		
Ra 14 z	0.09	13.07	10.34	1.55	3.14	28.04		5.93	671.30		
Ra 01 x	0.07	18.68	15.51	0.38	3.41	46.93	51.75	8.26	545.48		
By 04 x		16.43	17.50	1.04	3.05		73.68	6.07	765.64		
By 04 y		16.89	34.70	0.82	3.28	31.56	116.23	6.07	749.14		
By 04 z	2.8	16.65	12.01	0.41	2.68	41.15	84.11	6.07	466.62		
By 05 y	0	11.54	14.52	0.05	4.14	82.30	35.51	15.84	455.83		
Ma 11 x	Tidal		12.15	16.92	0.00	3.99	22.25		11.19	660.80	
Ma 11 y			13.20	20.81	0.00	4.19	7.82		12.49	572.66	
Ma 11 z		0.02	12.26	15.14	0.00	4.12	42.66		8.12	517.50	
Ra 15 x		0.13	15.45	11.20	0.86	3.84	50.30	10.15	10.18	675.97	
Ra 15 y			21.55	8.10	2.94	3.35	41.68		8.63	503.54	
Ra 15 z			21.15	6.84	0.87	3.49	37.85		7.33	479.77	
Ra 16 x			20.23	9.23	0.49	3.39	82.59		14.05	257.41	
Ra 16 y			20.70	5.89	1.93	3.55	66.42		11.53	273.31	
Ra 16 z		0.19	19.36	11.23	0.07	3.74	236.13	96.27	28.68	85.90	
By 13 x			18.31	7.16	1.33	3.76	72.14		13.21	432.02	
By 13 y			21.58	9.31	0.49	3.76	36.06		7.78	442.02	
By 13 z		0.10	15.91	5.00	2.16	4.25	19.29	54.99	3.07	422.02	
By 14 x		0.01	13.37	10.66	0.07	4.18	19.65	17.70	2.63	543.91	
By 14 y		14.39	18.14	0.43	4.14	6.44		1.93	481.03		
By 14 z		9.48	34.40	0.00	4.78	143.59		13.61	708.39		
By 15 x		21.40	5.54	4.00	2.48	48.83		10.45	546.05		
By 15 y		19.77	3.55	4.27	3.74	76.21		15.06	553.01		
By 15 z	0.36	19.78	4.80	3.48	3.01	46.50	124.10	9.20	573.31		
By 16 x		20.58	8.06	0.00	4.01	26.06		5.36	726.25		
By 16 y		20.45	7.96	0.10	4.44	25.97		5.31	531.07		
By 16 z	0.07	20.75	7.87	0.20	3.85	21.40	62.87	4.44	335.90		
By 18 y		17.01	6.97	1.57	3.07	43.24		6.70	406.80		
By 18 z	0.04	17.36	7.02	1.29	3.17	22.93		4.20	497.81		
By 19 x		16.98	15.67	0.00	3.96	22.64		3.78	620.84		
By 19 y	0.04	15.49	16.93	0.00	4.34	17.98	19.85	3.07	570.97		
By 19 z		18.32	22.50	0.00	4.09	43.31		5.68	519.22		
Ra 02 y	0.11	16.35	11.67	0.09	3.60	35.79	57.34	7.43	549.19		
Ra 04 x		23.72	9.51	1.24	3.64	20.73	90.28	5.86	549.90		
Ra 04 y		16.70	10.83	1.71	4.17	41.75	68.21	5.86	781.86		
Ra 04 z	0.16	16.42	15.45	0.04	4.03	27.09	54.54	5.86	545.00		
By 08 x	0.11	15.90	6.43	0.00	3.62	42.56	80.02	5.61	692.63		
By 09 x		18.33	19.16	0.64	3.43	54.94	51.05				
By 09 z	0.10	19.98	13.76	0.00	3.51	63.29	47.76				

Table 3

Summary of the minimum, mean, median and maximum values of each parameter measured in each sub-facies. G.I.: Grain interpenetration, C.I.F: Capillary Imbibition Factor.

Sub-facies	Value	Permeability (mD)	Porosity (%)	Cement (%)	G.I. (%)	V _p dry (km/s)	Formation factor	C.I.F. (g cm ⁻² h ^{-1/2})	Tortuosity	Mean grain size (μm)
Prograding Oolitic Lobe	Min	0.03	7.75	1.00	0.23	3.47	23.55	6.71	4.72	323.08
	Mean	1.28	16.11	6.30	0.90	4.37	62.65	54.83	8.88	482.24
	Median	0.13	15.71	4.70	0.60	4.38	47.44	33.61	7.88	440.85
	Max	8.94	27.59	14.01	2.33	5.67	241.51	128.49	14.05	792.56
Oolitic Shoal	Min	0.00	10.21	2.81	0.05	2.68	12.55	1.91	2.12	302.42
	Mean	0.43	15.32	10.40	0.87	3.50	54.56	58.10	7.88	488.51
	Median	0.15	16.43	9.37	0.82	3.56	47.46	61.49	7.59	451.25
	Max	2.80	18.68	34.70	2.12	4.22	157.26	116.23	18.63	806.60
Tidal	Min	0.01	9.48	3.55	0.00	2.48	6.44	10.15	1.93	85.90
	Mean	0.11	17.71	11.63	0.92	3.78	48.78	54.59	8.33	535.36
	Median	0.10	18.31	9.51	0.43	3.76	41.68	54.77	7.33	545.00
	Max	0.36	23.72	34.40	4.27	4.78	236.13	124.10	28.68	781.86

4.2. Diagenetic phases recorded in the Oolithe Blanche Formation

Eleven, sometimes overlapping, diagenetic phases were observed in the *Oolithe Blanche Formation*. These phases are either (bio)chemical (micritisation, grain dissolution, four types of cementation, dolomitisation and dedolomitisation) or physical (spalling, grain interpenetration and finally, fracturing). Some stylolitisation may be present, but is very rarely observed in this formation. A summary of the diagenetic sequences observed in each sample is presented in Figure 3, together with stratigraphy, sample position and sub-facies distribution.

Micritisation of ooids and bioclasts is associated with the creation of mouldic porosity after organic matter degradation and aragonite dissolution (Fig. 4A and B). Four types of cementation are present: isopachous (and palissadic), syntaxial, blocky calcite 1 (BC1) and blocky calcite 2 (BC2). Isopachous cementation appears as a fringe of fibrous calcitic cement about 5–10 μm wide, growing perpendicular to the substratum. It can be found in interparticle porosity but also in intraparticle porosity in the case of grain dissolution. Palissadic cements about 10–15 μm in length are also observed. All isopachous and palissadic cements show light pink to pale mauve staining (Fig. 4C).

The second phase of cementation consists of a syntaxial calcite, which is an overgrowth around fragments of echinoderms. Both staining (Fig. 4D) and cathodoluminescence (Fig. 4E and F) show the presence of a thin, banded succession of stripes (Fig. 4D).

Two blocky calcite cements (Fig. 4G and H), both sparitic, are differentiated. The first type of blocky calcite (BC1) shows variable colouring under cathodoluminescence, with red and orange zonation that may also sometimes be yellowish. After calcite staining, it displays pink to red colouring. The second type of blocky calcite (BC2) is brown and shows no zonation under cathodoluminescence. After calcite staining, it displays pink to mauve colouring. Finally, the presence of pores with rhombohedral geometry and the truncation of particles or late blocky calcite cements indicate the existence of dolomitisation and dedolomitisation phases (Fig. 5A and B).

The next three phases relate mainly to physical diagenesis, induced by lithostatic compaction during burial directly related to basin subsidence.

Spalling is observed in several samples and occurred when lithostatic compaction brought at least two grains into contact. Under compression, the concentric envelope forming the cortex of the ooids became detached (Fig. 5C and D). Space between spalling and the remaining ooid cortex is always filled with BC1.

Another important diagenetic feature induced by compression is grain interpenetration. During compaction, some grains formed concavo-convex or tangential contacts (*sensu* Flügel, 2004).

Although rarely observed, micro-stylolites are occasionally found at the interface between two interpenetrated grains.

Compaction may also lead to micro-fracturing. Most of the fracturing is observed in the Prograding Oolitic Lobe sub-facies and is always filled with BC2 (Fig. 5E and F). Note that this fracturing observed at thin-section scale is less than 10 μm wide. No macroscopic fractures are observed.

4.3. Characterisation of the pore network

A summary of the petrophysical parameters measured is presented in Table 2. Micropores are observed mainly in ooids but are also present in micritised grains. Mesopores are less common and are always found in interparticle porosity. Macropores are rarely observed, are always mouldic and related to dedolomitisation. Porosity values range from 7.7% to 27.6%, with a mean value of 16.6% for all samples. The highest mean and median values are observed in the Tidal sub-facies (Table 3).

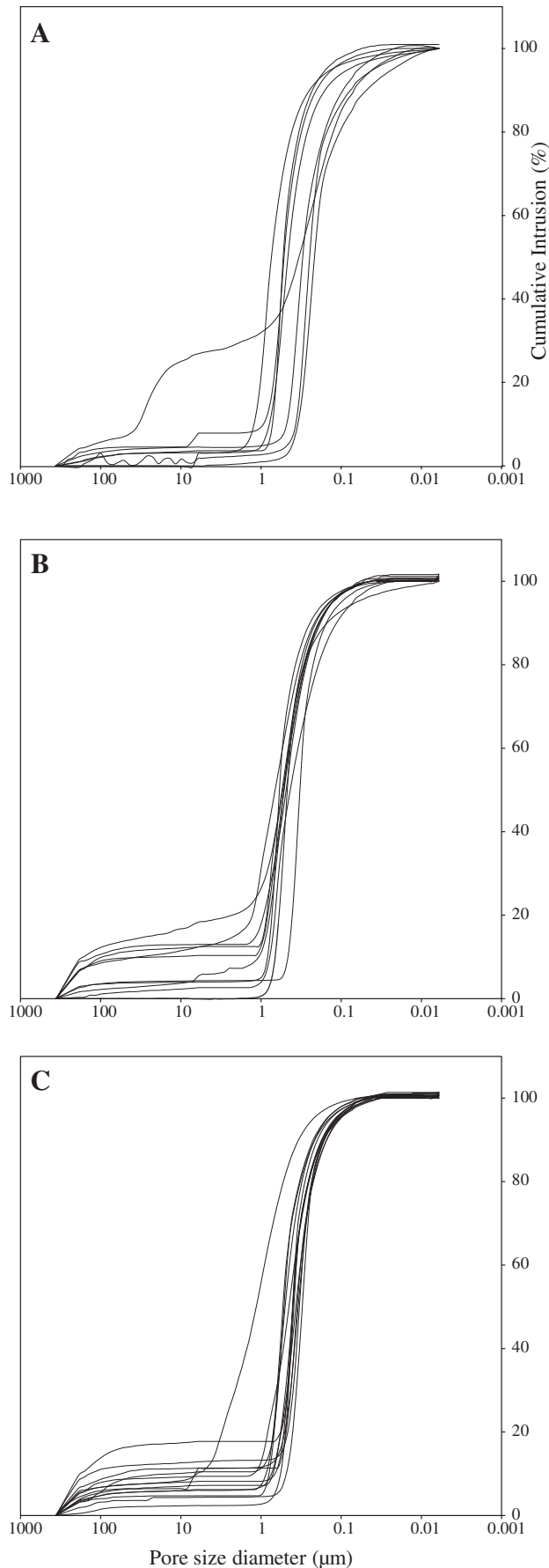
Mercury injection porosity measurement shows an average pore-throat diameter of 0.23 μm, with no discrimination among the three sub-facies (Fig. 6), with the exception of sample MA01 (in the Prograding Oolitic Shoal sub-facies) with two pore-throat categories.

The values of the formation factor range from 6.4 to 241.5. While the Prograding Oolitic Lobe and Oolitic shoal sub-facies show similar median (47.4 and 47.5 respectively) and mean values (62.7 and 54.6 respectively), the lowest values are observed in the Tidal sub-facies (mean 48.8 and median 41.7). Calculated tortuosity values range from 1.93 to 28.68. The Prograding Oolitic Lobe sub-facies shows the highest mean values (8.9) while the lowest values are observed in the Oolitic Shoal sub-facies (7.9). Median values are similar in the Prograding Oolitic Lobe and the Oolitic Shoal sub-facies (7.9 and 7.6 respectively) while the lowest values are found in the Tidal sub-facies (7.3).

Seven plugs were submitted to an extensive nano-CT scan investigation. From these analyses, we present 2D reconstructions (Fig. 7) for samples BY 08x and BY 13y (Tidal sub-facies). Comparison of the connected pore network shows major differences between the two samples. Sample BY 08x shows a strongly connected pore network with a large, central connected zone, whereas BY 13y shows several connected zones that are not mutually interconnected.

4.4. Fluid-flow characterisation and acoustic properties

The overall permeability of the reservoir is low with values ranging from 0.001 mD to 8.94 mD (Table 2) and a mean value of 0.36 mD. Median values (Table 3) are similar for the three sub-



facies while mean values range from 1.28 mD in the Prograding Oolitic Lobe sub-facies to 0.11 mD in the Tidal sub-facies. Only sample BY01 shows a higher permeability (8.94 mD).

Capillary Imbibition Factor values range from $6.7 \text{ g cm}^{-2} \text{ h}^{-1/2}$ – $128.5 \text{ g cm}^{-2} \text{ h}^{-1/2}$. The Prograding Oolitic Shoal sub-facies shows considerable variability. The highest median value is observed in the Oolitic Shoal sub-facies (Table 3).

Measured velocities vary between 5.67 km s^{-1} and 2.48 km s^{-1} (Table 2). Both the Oolitic Shoal and the Tidal sub-facies show the lowest V_p values (mean 3.50 and 3.78 km s^{-1} , median 3.56 and 3.76 km s^{-1} , respectively) while the Prograding Oolitic Lobe sub-facies shows the highest values (mean 4.37 km s^{-1} , median 4.38 km s^{-1}).

4.5. Statistical analyses

The PCA analysis and its associated Pearson correlation table show several relationships between key parameters. Positive and negative correlations are illustrated in the PCA circle of correlation (Fig. 8), where positively correlated variables tend to be close while negatively correlated variables tend to be diametrically opposed in the projections. Principal components 1 and 2 (Fig. 8A) represent 48% of the total variability (27.5% and 21.1% respectively) and the projections on axes 1 and 3 (Fig. 8B) represent 45% of the total variability.

The Pearson product–moment correlation coefficient indicates the linear dependence between two variables. Table 4 shows the r -value and its associated p -value. For p -values below 0.05, the correlation is statistically significant.

Six strong positive correlations are highlighted: (i–ii) permeability with interparticle cement area and with capillary imbibition factor, (iii) porosity with capillary imbibition factor, (iv–v) formation factor with V_p and with tortuosity and finally (vi) mean grain size with interparticle cement area. Five strong negative correlations are also present: (i–iv) V_p with permeability, porosity, capillary imbibition factor, or grain interpenetration and (v) grain interpenetration with interparticle cement area.

Identifying sub-facies on cross-plots confirms the PCA. The permeability vs porosity cross-plot (Fig. 9) shows a positive correlation, while no discrimination is possible between sub-facies. Capillary imbibition factor vs porosity (Fig. 10) shows a strong positive correlation, as demonstrated by the PCA. The permeability vs grain interpenetration cross-plot (Fig. 11) shows no correlation, and no trends in sub-facies. Samples from the Tidal sub-facies with isopachous cementation always have low grain interpenetration values in the case of low to medium permeability.

The V_p vs porosity cross-plot (Fig. 12) shows a strong negative correlation. Unique trends are also observed in the sub-facies. At fixed porosity, the three sub-facies can be sorted by grading velocities in this order: Oolitic Shoal, Tidal and Prograding Oolitic Lobe. To further investigate sub-facies discrimination, the study of each group individually reveals a significant negative correlation between porosity and V_p ($p < 0.05$). Least squares estimates of slope and intercept couples, together with their 95% joint confidence regions, are plotted in Figure 14 (see Cornillon and Matzner-Løber, 2007 for more detail about calculation).

For the LDA, our dataset was composed of 58 samples for which all the parameters have been measured. The associated Wilks Lambda value is 0.31 and the associated F value is 4.1386. For $\alpha = 0.01$, the critical F value is 2.13 with degrees of freedom of 18 and 94. The LDA indicates that 69% of the samples (i.e. 40 samples)

Figure 6. Mercury injection porosimetry measurement in the three sedimentological sub-facies. (A) Prograding Oolitic Lobe, (B) Oolitic Shoal and (C) Tidal sub-facies.

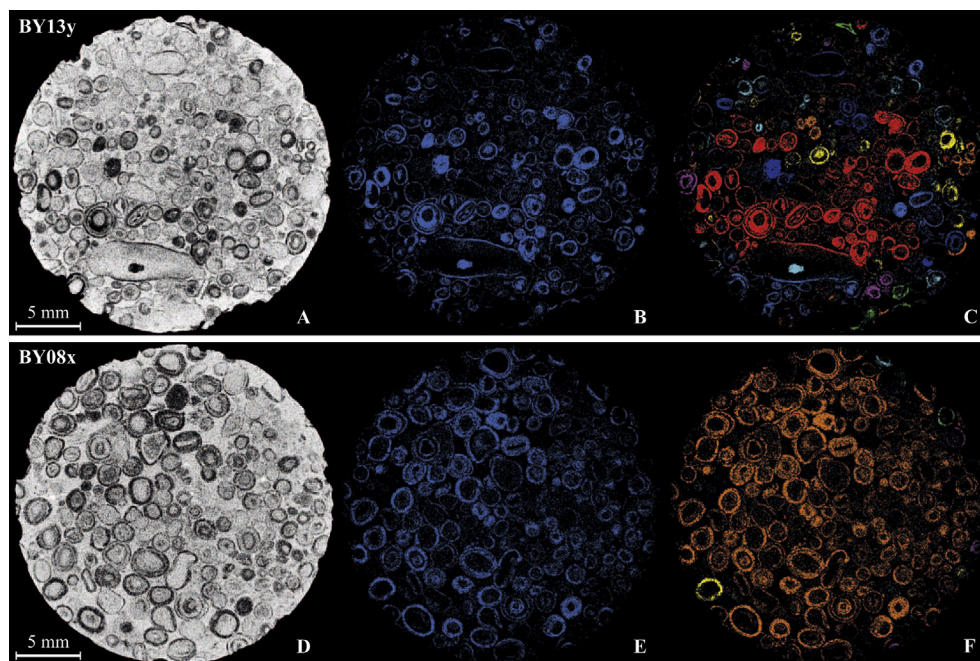


Figure 7. Orthoslices from Nano CT-scans analyses for samples BY13y (A, B and C) and BY08x (D, E and F). A and D are the raw CT-scans. B and E represent the porosity network (blue) after threshold on the mineral matrix (black). C and F represent the connectivity of the pore network. Porosity zones of the same colour are connected. BY13y exhibits several zones of micropore connectivity which are not interconnected. BY08x exhibits a large zone where the entire intraparticle micropore system is connected. (For interpretation of the references to colour in this figure legend, the reader is referred to the web version of this article.)

are well categorised by sub-facies, as determined in the field (Table 5).

5. Discussion

5.1. Sedimentary model of the Oolithe Blanche Formation

By integrating field observations with depositional models derived from recent systems such as the Great Bahamas Bank (Harris, 1979; Harris et al., 1979; Reijmer et al., 2009; Reeder and Rankey, 2008, 2009; Rankey and Reeder, 2010, 2011), a simplified sedimentary model has been developed, showing the distribution of sub-facies in the *Oolithe Blanche Formation* (Fig. 13).

The grainstone texture and the sedimentary structures observed in the Oolitic Shoal sub-facies indicate shallow, high-energy shoreface depositional environments, permanently subjected to relatively high-energy, uni-directional currents, as can be observed today in oolitic shoals. For the Tidal sub-facies, the limestone texture and the sedimentary structures are typical of a shallow, high-energy tide-dominated shoreface environment. Finally, in the Prograding Oolitic Lobe sub-facies, the dominant grainstone (and packstone), the poorly sorted deposits and the local occurrence of a matrix all indicate a shallow, agitated environment with moderate to high-energy currents. Typical sedimentary structures such as sigmoidal ripples indicate the dominance of tidal currents. These large sedimentary structures are interpreted as horizontally and vertically stacked flood lobes, extending in tidal channels, in an internal position relative to the oolitic shoals.

5.2. Paragenesis of the reservoir

The paragenesis of the *Oolithe Blanche Formation* is presented in Figure 14. The earliest diagenetic phase, micritisation (affecting ooids and bioclasts), is observed mainly in shallow marine environments and may occur directly on, or just below, the seafloor.

Mouldic porosity created by organic matter degradation and aragonite dissolution is filled by drusy calcite crystals increasing in size towards the centre of the pore (Flügel, 2004). Early aragonite dissolution in marine phreatic environments is a recognised phenomenon in calcitic seas, notably during the Jurassic (Sandberg, 1983).

When present, isopachous cements form a coating around allochems. Staining of isopachous cement indicates a non- to weakly ferroan calcite and thus a marine phreatic environment (Tucker et al., 1990). Syntaxial calcite overgrowth must have begun at the same time, as shown by the absence of isopachous cementation around echinoderm fragments. Syntaxial cement also points to a marine phreatic diagenetic environment.

Where isopachous cements exist, they fringe any spalled rims, showing that this type of cementation occurred before compaction. When isopachous cements are absent, the spalled rims are surrounded by blocky calcite. Grain interpenetration is rarely present in samples where isopachous cementation occurred. An isopachous fringe has sometimes been preserved between interpenetrated grains (Fig. 5D). The mechanism involved in grain interpenetration is probably related to pressure-dissolution. Compaction therefore occurred after the precipitation of isopachous cement and before the onset of blocky calcite cementation.

Under cathodoluminescence, BC1 shows zonations, indicating chemical modifications of the parent fluids during crystallisation. The pink to red colouring after calcite staining corresponds to non-ferroan calcite. This type of cementation followed syntaxial overgrowth (Fig. 4F). Micro-fracturing cross-cuts all the diagenetic features described so far. Then the second type of blocky calcite filled any remaining porous space. BC2 shows no zonation under cathodoluminescence, which could indicate diagenetic fluid with a stable chemical composition during precipitation. Calcite staining (pink to mauve) indicates a non- to slightly ferroan calcite showing that the later diagenetic environment of BC2 was more reductive and deeper (Lindholm and Finkelman,

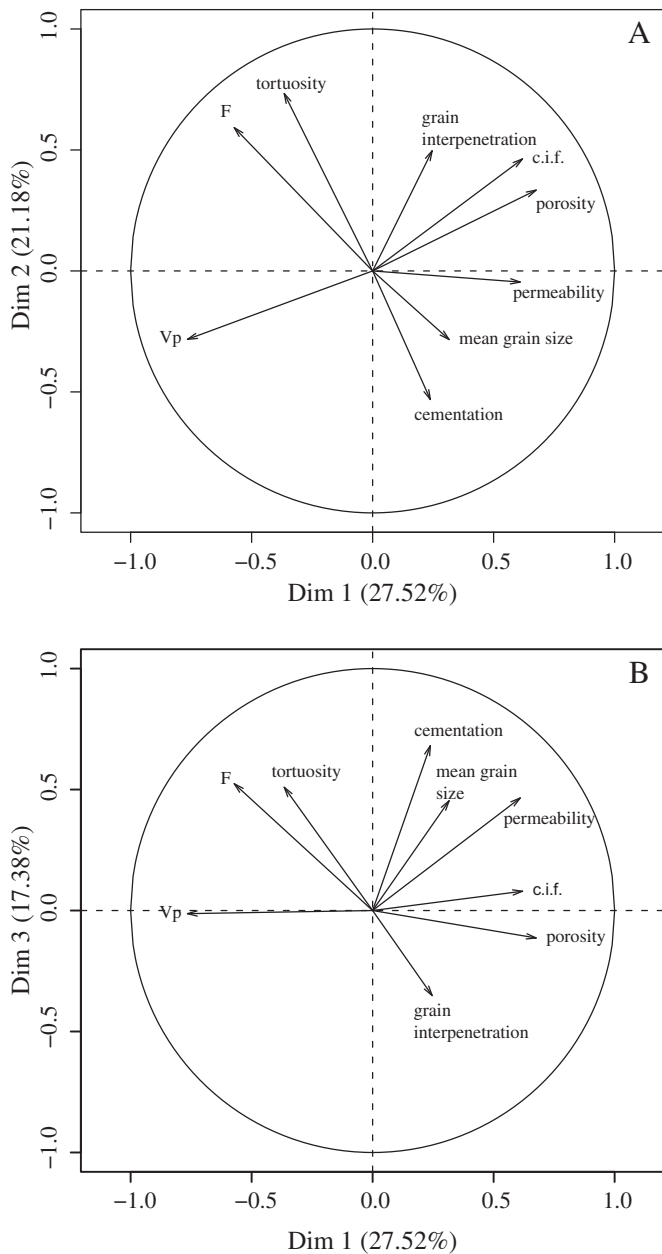


Figure 8. A PCA projection of the variables studied on the principal axes 1 and 2 (A) and axes 1 and 3 (B). Strong positive correlations between variables are highlighted by their proximity. Diametrically opposed variables are strongly negatively correlated.

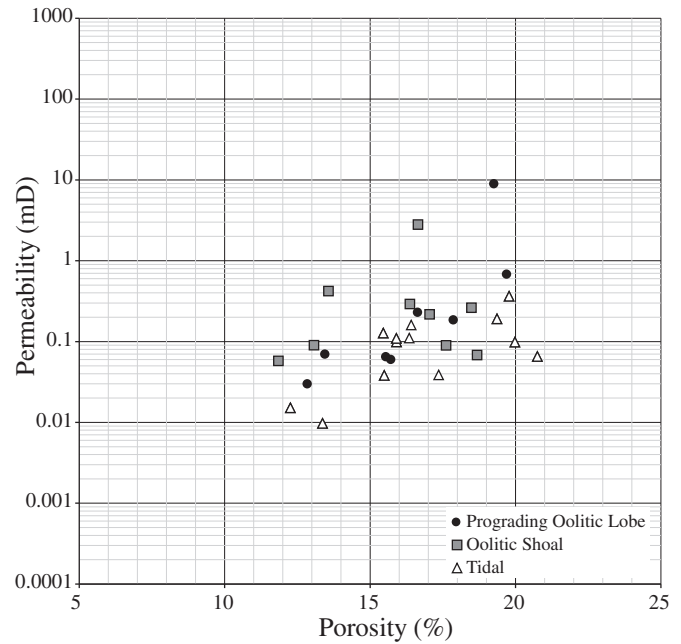


Figure 9. Permeability vs. porosity cross-plot.

1972). Blocky calcite cements precipitated in the open primary and secondary porosity, during mesogenesis and burial. The timing of dolomitisation and dedolomitisation is still unclear. As rhombohedral macropores cross-cut every previously mentioned diagenetic feature, whether (bio)chemical or physical, dolomitisation and dedolomitisation must intervene at the end of the sequence, during telogenesis.

Subtle differences can be observed between the three sub-facies. In the Tidal sub-facies, grain sorting is almost always homogeneous and the grain interpenetration surface is the greatest. Dolomitisation is absent. This sub-facies presents the highest content of isopachous cements and the largest surface of cementation (Tables 2 and 4).

The Oolitic Shoal sub-facies, dominated by ooids with minor bioclasts, has almost the same diagenetic history as the Tidal sub-facies. The only difference is that isopachous cementation is rarely observed (with the exception of one sample, RA01).

Dolomitisation and dedolomitisation are only observed in the Prograding Oolitic Lobe sub-facies in the Massangis quarry. All the samples display some dedolomitisation, and macroporosity ranging from 1.2 to 8.9% (Casteleyn et al., 2010a; quantified from image analysis). Spalling is rarely observed and grain sorting is always heterogeneous.

Several authors, including Shearman et al. (1970), have shown that the formation of an ooid is partially due to the presence of

Table 4

Pearson correlation coefficient calculated with the diagenetic and petrophysical measurements for all the datasets. In bold, *p*-values < 0.05 and associated *r*-values. G.I.: Grain Interpenetration, C.I.F.: Capillary Imbibition Factor, M.G.S.: Mean Grain Size.

	Permeability	Porosity	Cement	G.I.	VP dry	Formation Factor	C.I.F.	Tortuosity	M.G.S.
Permeability		0.1350	0.3724	0.0048	-0.4230	-0.1084	0.3821	-0.0874	0.2035
Porosity	<i>p</i> = 0.312		-0.0916	0.1932	-0.5167	-0.2428	0.4739	-0.0005	0.1937
Cement	<i>p</i> = 0.004	<i>p</i> = 0.494		-0.3549	-0.0859	-0.1105	-0.0420	-0.1108	0.4198
G.I.	<i>p</i> = 0.972	<i>p</i> = 0.146	<i>p</i> = 0.006		-0.2586	-0.0357	0.1908	0.0933	0.0367
VP dry	<i>p</i> = 0.001	<i>p</i> = 0.000	<i>p</i> = 0.522	<i>p</i> = 0.049		0.2594	-0.4362	0.0226	-0.0339
Formation Factor	<i>p</i> = 0.418	<i>p</i> = 0.066	<i>p</i> = 0.409	<i>p</i> = 0.790	<i>p</i> = 0.049		-0.0455	0.8637	-0.1155
C.I.F.	<i>p</i> = 0.003	<i>p</i> = 0.000	<i>p</i> = 0.754	<i>p</i> = 0.151	<i>p</i> = 0.001	<i>p</i> = 0.735		0.0868	-0.0163
Tortuosity	<i>p</i> = 0.514	<i>p</i> = 0.997	<i>p</i> = 0.407	<i>p</i> = 0.486	<i>p</i> = 0.866	<i>p</i> = 0.000	<i>p</i> = 0.517		-0.0549
Mean Grain Size	<i>p</i> = 0.125	<i>p</i> = 0.145	<i>p</i> = 0.001	<i>p</i> = 0.785	<i>p</i> = 0.801	<i>p</i> = 0.388	<i>p</i> = 0.903	<i>p</i> = 0.682	

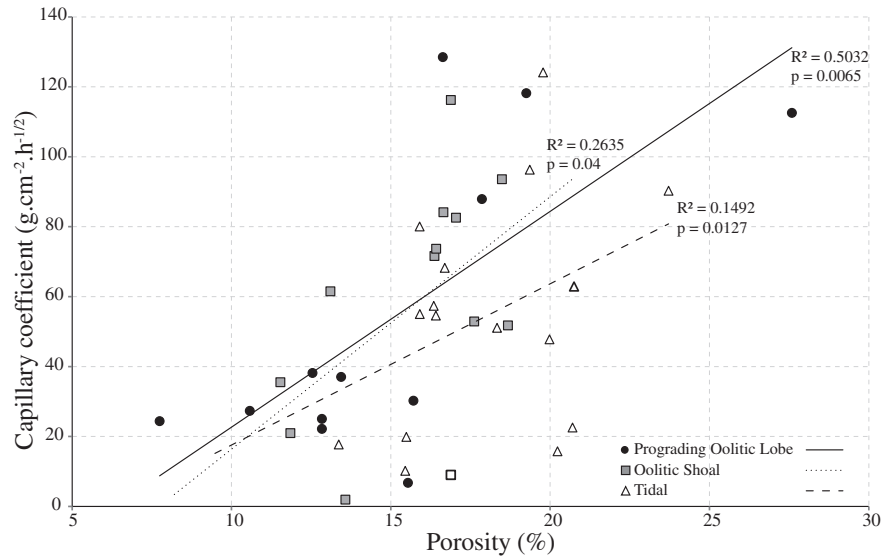


Figure 10. Capillary imbibition factor vs. porosity cross-plot.

algae, leaving organic matter inside the cortex and participating in the structuring of the lamination. Even though the processes involved in the formation of the cortex are still debated (Pacton et al., 2012), studies of recent deposits in Bahamas (Duguid et al., 2010) suggest that microorganisms do not participate in cortex formation. According to some authors, degradation of organic matter contained in the cortex of ooids could lead to the creation of micropores (Harris et al., 1979; Purser, 1983). The origin of intra-particle micropore network development therefore still requires further investigation.

5.3. Factors controlling fluid flow and acoustic properties

Permeability vs. porosity (Fig. 9) and capillary imbibition factor vs. porosity (Fig. 10) show trends similar to those previously

described in the literature (e.g. Worthington, 1993), i.e. an increase in both these parameters as porosity increases. Permeability and porosity are correlated but, for a given porosity value, permeability values vary considerably, therefore no significant correlation can be determined by statistical methods. This is common in carbonate reservoirs where heterogeneity in terms of microstructure induces a complex relationship between permeability and porosity (Rezaee et al., 2007; Palermo et al., 2010). Fracturing may also have an important effect on the porosity–permeability relationship, but in our case the “micro”-fracturing observed does not affect reservoir permeability.

David et al. (2011) also proved that capillary imbibition could be used as a proxy to describe rock permeability. For the capillary imbibition factor vs porosity cross-plot, the three sub-facies cannot be discriminated and do not display distinct trends (some overlap occurs at the highest and lowest porosity values). The variations in permeability encountered in this reservoir could explain the wide range of values for the Capillary Imbibition Factor.

A rather unexpected result is highlighted by the PCA: the cementation area is positively correlated both to grain size and to permeability.

Different packing arrangements for uniform spheres have a major impact on interparticle porosity. While a rhombohedral or “closed-packed” system has a porosity of 25.9%, a cubic or “wide-packed” system has an interparticle porosity of 47.6% (Graton and Fraser, 1935). Original porosity for oolitic and bioclastic sand is estimated at 40% (Lucia, 2007; Zinszner and Pellerin, 2007). Different grain sizes will disturb packing, thus increasing interparticle porosity (Tiab and Donaldson, 2012).

Petrographic observation indicates that the presence of non-spherical particles also disturbs grain-packing. In comparison to ooids and pellets, which are spherical and tend to have constant radii, skeletal particles show great morphological variability. Therefore, a high mean grain-size value reflects a high proportion of skeletal particles such as bioclasts.

The presence of skeletal particles of various forms increases interparticle porosity, which will later be filled by cementation. Skeletal particles, such as echinoderms, also represent ideal nucleation sites (Flügel, 2004). With a greater number of skeletal particles in the fabric, more space remains available for later cementation, thus explaining the positive correlation between grain size and cementation area.

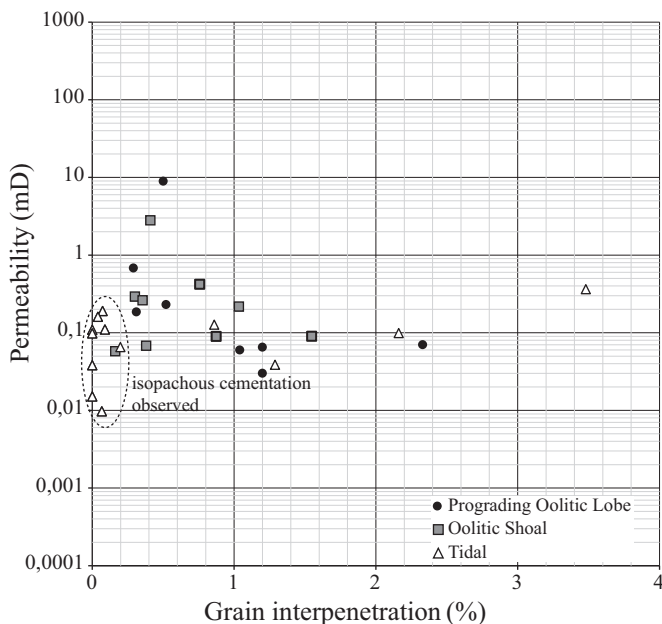


Figure 11. Permeability vs. grain-interpenetration cross-plot. The dashed encircled zone contains samples with isopachous cements.

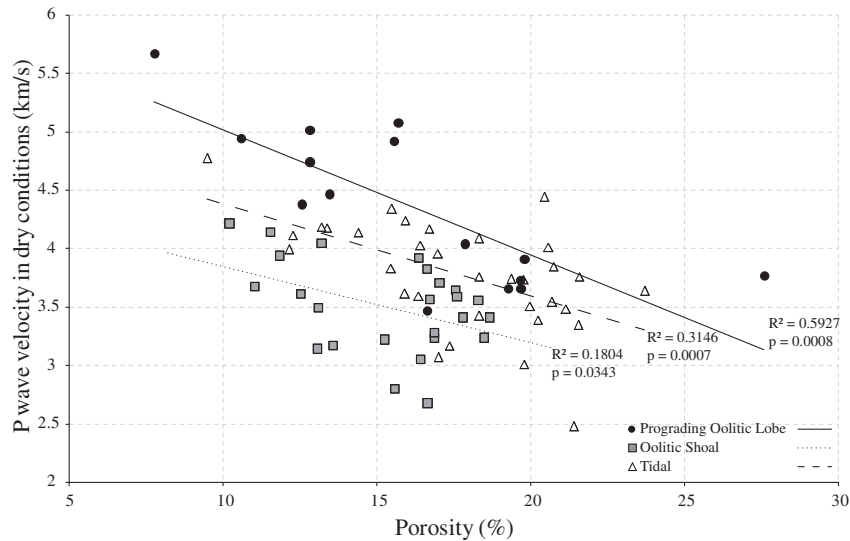


Figure 12. P-wave velocity vs. porosity cross-plot.

Surface contact between grains is greater in ooid and bioclast arrangements than in ooid-only arrangements, as bioclasts have larger contact surfaces, which are microporous due to early micritisation. This extended contact within an intraparticle micropore network could explain the positive correlation between permeability and cementation area.

The negative correlation between interpenetration and cementation (Fig. 8A) needs to be considered in terms of diagenetic history. In cases where cementation intervenes in the earliest types of diagenesis, as with isopachous cements, the cement coating formed around the grain prevents interpenetration during later compaction, because it serves as a stabilising framework. When compaction occurs earlier than cementation, the volume of primary porosity, i.e. the space available for cementation, decreases.

Casteleyn et al. (2010a) showed that the micropore network became connected through the ooids, thus improving the permeability of the rock. However, the permeability vs. grain interpenetration cross-plot (Fig. 11) shows no relationship between these two parameters in our study. No obvious trends can be discerned for any of the sub-facies. Nevertheless, by taking into account the paragenesis of each sample, the cross-plot can be shown to reflect the role of cementation in fluid-flow properties. Isopachous cementation is mainly present in the Tidal sub-facies. Permeability values measured in samples with isopachous cementation are low (dashed zone). When isopachous are absent, samples can show higher values of permeability. The Oolitic Shoal has better permeability than the other two sub-facies. Although it has lower porosity for an equivalent cementation area than the Tidal sub-

Table 5

Confusion matrix associated with the LDA. Each column represents the real number of samples labelled in a sub-facies, in the field. Each row represents the predicted number of samples reclassified in a sub-facies by the LDA. P.O.L.: Prograding Oolitic Lobe. For example, 21 samples from the Oolitic Shoal sub-facies were used (total of column#1). Of these 21, 17 were well-categorised in the "Oolitic Shoal" group defined by the LDA, 3 were categorised as Tidal and 1 as P.O.L.

Predicted	Real		
	Oolitic shoal	P.O.L.	Tidal
Oolitic Shoal	17	2	5
P.O.L.	1	7	5
Tidal	3	3	16
Well classed	80.9%	58.3%	64%

facies, its grain interpenetration is the highest, providing better connectivity for the intraparticle micropore network. The Prograding Oolitic Lobe sub-facies is the only one with mouldic macroporosity after dedolomitisation and should therefore display better permeability. Mercury injection porosimetry shows that the average pore-throat diameter is about 0.23 μm , meaning that even if mouldic macroporosity is present, it will be connected to the pore network via interparticle microporosity, providing no enhancement of reservoir quality.

Nano-CT scan analyses on intraparticle micropore systems remain scarce but recent studies have proved their efficiency in providing information on pore distribution (Van Geet et al., 2003). However, the major issue concerns the resolution attainable. The pore network studied here is dominated by intraparticle microporosity (<1 μm), with an average pore-throat diameter of 0.23 μm , while the lowest resolution achieved was 1.5 $\mu\text{m}/\text{voxel}$. Therefore micropore network reconstruction from nano-CT scans describes both the porosity aggregation area and zones of dense pore presence. One way to overcome this technological issue is to link image analyses to petrophysical properties. Tortuosity is one of the most important parameters when assessing fluid-flow properties in reservoirs but remains difficult to quantify (Verwer et al., 2011). Two samples from the same sub-facies were scanned and reconstructed (Fig. 7). The diagenetic and petrophysical properties of these two samples are summarised in Table 2. While sample BY 13y is more porous and more cemented with more interpenetrated grains, it has almost the same permeability value as sample BY 08x. Interestingly, sample BY 13y shows a tortuosity value higher than sample BY 08x (7.78 vs. 5.86 respectively). A closer examination of pore-network connectivity shows that sample BY 13y presents several zones where a few grains are connected together, creating small zones of connectivity, which are not inter-connected. In contrast, a large zone of connectivity exists in sample BY 08x, linking almost all the grains. Even though this sample is less porous, without interpenetrated grains, the connectivity of its pore network induces a low tortuosity value and creates a permeability similar to that of sample BY 13y.

As expected, V_p and porosity show a negative correlation (Fig. 12). Such results are in good agreement with published results for other carbonate reservoirs (e.g. Cole, 1976; Anselmetti and Eberli, 1993; Baechle et al., 2005, 2008; Croizé et al., 2010; Fournier et al., 2011). Similar trends are observed when

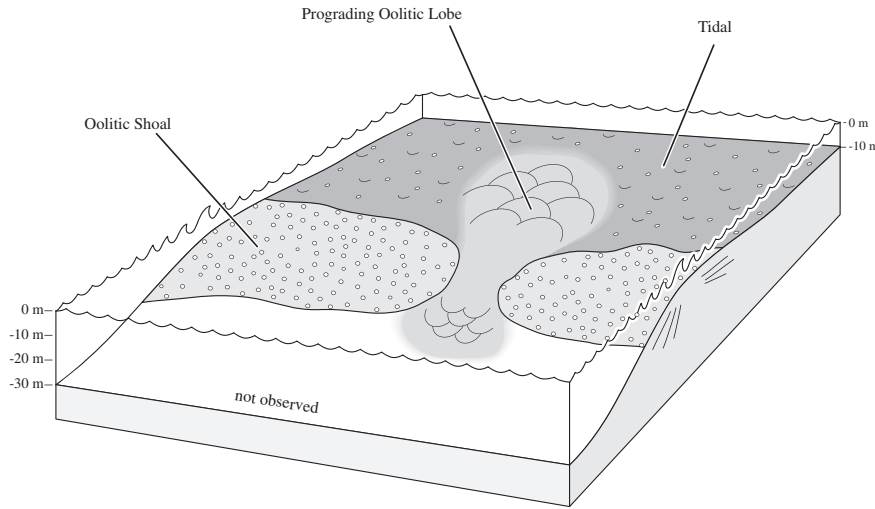


Figure 13. Sedimentary model and sub-facies distribution in the Oolithe Blanche Formation.

evaluating acoustic properties in water-saturated conditions. However, the lack of V_p measurement in saturated conditions for the Prograding Oolitic Lobe sub-facies prevents a complete cross-plot analysis. The negative correlation between V_p and the capillary imbibition factor is explained by the strong positive correlation between porosity and capillary imbibition. In addition there is a negative correlation between V_p and permeability, as permeability is correlated to capillary imbibition. Several authors have linked V_p with other parameters; Dvorkin et al. (1991, 1994) and more recently Croizé et al. (2010) demonstrated that amount and radius of cementation increase the stiffness of carbonate rocks and thus the acoustic velocities, inducing scattering in typical V_p vs porosity cross-plots. In addition, Rong et al. (2012) showed that V_p increases with an increase in mean grain diameter and Brigaud et al. (2010) showed that V_p tends to be greater in microporous carbonates where compaction starts before cementation, but lower in carbonates where cementation starts before compaction, especially when isopachous cementation is present.

Both cross-plot (Fig. 12) and least squares estimates of slope and intercepts (Fig. 15) show specific trends among sub-facies. Each ellipse appears different from the others. Moreover their position in Figure 15 suggests that the three linear regressions possess the same slope, but with different intercepts.

The Prograding Oolitic Lobe shows the highest velocities, which can be explained because it also has lower porosity, mean grain size, and cementation area than the other two sub-facies. Weger

et al. (2009) demonstrated that carbonates with larger pores have higher acoustic velocities than microporous carbonates. The Prograding Oolitic Lobe displays mouldic macroporosity in addition to intraparticle microporosity.

The Tidal sub-facies has higher porosity than the Oolitic Shoal sub-facies with isopachous cementation: it should therefore present lower acoustic velocities. The fabrics in the Oolitic Shoal and Tidal sub-facies are almost identical, with high ooid content and greater interparticle cementation area. However, the Tidal sub-facies presents higher mean grain size and smaller grain-interpenetration area. In the case of a carbonate where pore type is dominated by intraparticle microporosity, it appears that microstructure and diagenesis, inherited from the depositional environment, have a greater influence on acoustic velocities than porosity alone. This influence is similar to that of carbonate texture (Verwer et al., 2008; Fabricius et al., 2010).

Figure 16 summarises the relationship between the diagenetic features and petrophysical properties observed in the Oolithe Blanche Formation. Case A presents a sample where grain interpenetration or contact is null and therefore fluid migration is impossible, because interparticle porosity is filled with blocky calcite. In this case, cementation occurs before lithological compaction, with low to null permeability. In cases B and C, lithological compaction occurs before blocky calcite cementation. The

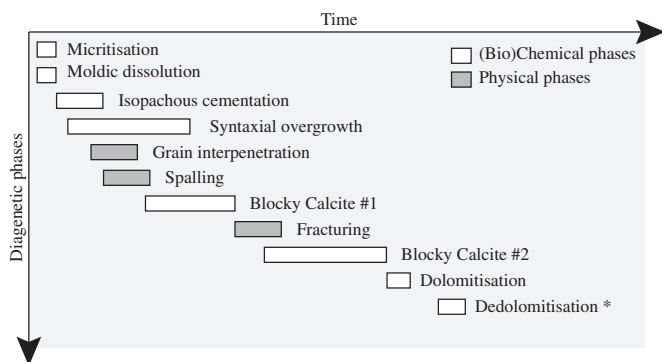


Figure 14. Relative chronology of diagenetic phases. *Dedolomitisation is only observed in the Prograding Oolitic Lobe sub-facies.

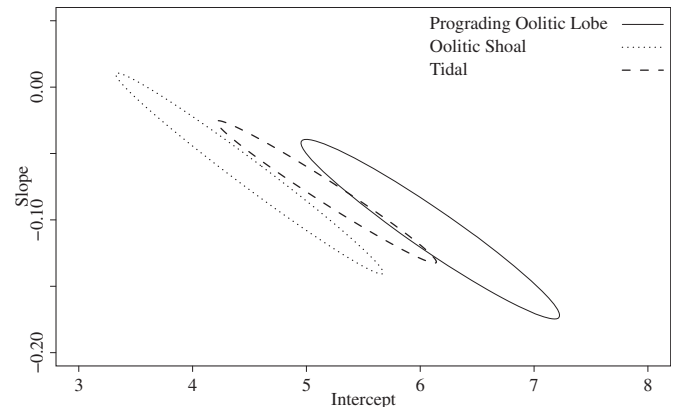


Figure 15. Joint confidence areas for slopes and intercepts of the linear regressions (95% confidence level) for each sub-facies considered separately.

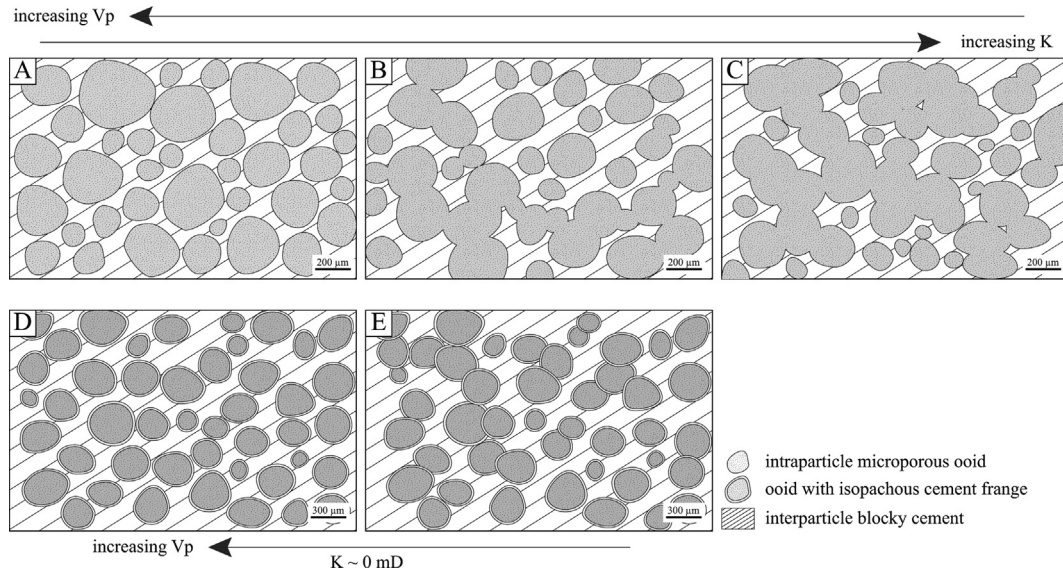


Figure 16. Sketches representing five cases observed in the *Oolithe Blanche* Formation. Total porosity is considered constant throughout. (A) Grainstone with microporous ooids where initial porosity is filled with blocky calcite cementation, grain contact is null. (B) Compaction has induced grain contact and grain interpenetration. (C) Compaction is greater, leading to greater surfaces of grain contact and grain interpenetration. In terms of permeability, cases can be organised as $C > B > A$. Measured V_p would be greater in case A than case C. (D) The same situation as case A but isopachous cementation is present around the ooids. (E) Isopachous cementation is followed by compaction, leading to isopachous cementation trapped during grain interpenetration. While permeability will be the same for D and E (near 0 mD), acoustic velocities would be greater in D.

surface of grain contact and grain interpenetration increases, thus facilitating interparticle micropore connectivity, creating paths for fluid migration. Case C presents a sample with intense grain contact and grain interpenetration, where fluid-flow properties are therefore the most efficient. In cases A, B and C, V_p tends to decrease as the path taken by acoustic waves becomes more complex. Finally, cases D and E present an alternative situation where the surface of grain contact and grain interpenetration is extensive but the presence of isopachous cementation prevents the connectivity of the interparticle micropores, inducing a shielding effect. Permeability is very low to null, and V_p tends to be lower than in case C, because the presence of isopachous cementation adds even more complexity to the travel path of the acoustic waves.

5.4. Sub-facies discrimination model

Few authors have developed methods to predict depositional facies or petrophysical properties in carbonate reservoirs, especially for sub-surface data (e.g. Qi et al., 2007; Verwer et al., 2009). The development of such methods will have a considerable impact on carbonate reservoir exploitation (Burchette, 2012). In our study the amount of data collected and the complexity of the relationships between variables make it imperative to use a statistical method to assist in sorting samples by their properties.

Of the 58 samples in our dataset, the LDA correctly categorised 40 in their specific sub-facies. Figure 17 shows the projection of our samples on the two discriminant axes. While a certain degree of discrimination can be observed, some samples tend to plot at the limit between two groups. There are two possible hypotheses to explain these remaining 18 samples. The first hypothesis concerns intrinsic natural variability that can neither be accessed nor explained by this test. The second hypothesis is related to the sampling process. During sampling, a block could be taken from the transitional zone between two different sub-facies, with samples therefore exhibiting properties from each of them.

The model derived from our methodology confirms the strong link between sedimentological, diagenetic and petrophysical properties. Such a model can be predictive, i.e. a full set of new samples of unknown sub-facies type can be processed and categorised with this tool. Geothermal energy exploitation in the Paris Basin and particularly in the *Oolithe Blanche* Formation requires thorough 3D modelling of the lateral and horizontal heterogeneities in reservoir properties.

Our field model is the first step in a broader programme concerning the Paris Basin. This model may serve as a basis to predict sub-facies distribution in several cores, with implementation of the same diagenetic and petrophysical investigations. After testing our model on several cored wells, the same methodology may be deployed at basin scale, with well-logs as the initial data. It will therefore become possible to predict reservoir heterogeneities, thus enhancing 3D basin models used for geothermal well

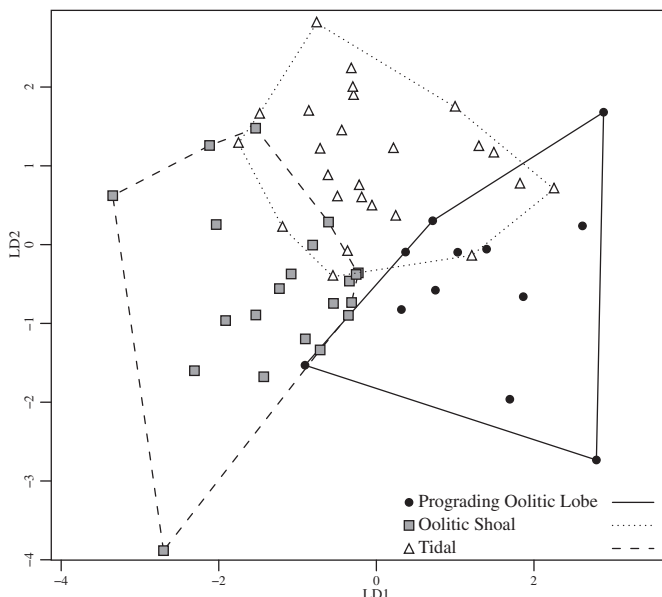


Figure 17. LDA model computed from diagenetic and petrophysical measurements.

implementation. Not only will our model facilitate future studies, its methodology will also be transposable to similar complex carbonate reservoirs and even non-oolitic reservoirs.

6. Conclusion

The *Oolithe Blanche Formation* forms a complex, tight carbonate reservoir, showing heterogeneous petrophysical properties. This paper emphasises the impact of the depositional setting and the diagenetic overprint on these heterogeneities.

Fluid-flow properties in this reservoir are related to the connectivity of the intraparticle micropore network. Intraparticle micropores also connect mouldic macropores, if present. Early cementation (via isopachous cementation) induces a lack of connectivity in the interparticle micropore network and thus explains to some extent the very low permeability encountered. Early compaction, with the development of grain interpenetration, permits better connectivity in the pore network, leading to better reservoir properties.

Grain size and bioclast content have an impact on permeability. As ooid packing during compaction is disturbed by the presence of bioclasts, it leaves more initial interparticle porosity to be filled by later cementation. It also increases the surface contact between intraparticle microporous grains. For a long time, permeability was mainly linked to porosity and pore type. Our study demonstrates that in addition to pore type, microstructural parameters (e.g. grain size and grain composition) need to be assessed. The same statement applies to acoustic properties.

All these observations relate to the complexity of the pore network, or tortuosity. Pore network characterisation coupled with CT scan analysis together show that tortuosity is a key parameter to investigate, as it may explain heterogeneities in the permeability values measured.

The complexity of the reservoir studied and the amount of data collected have led us to develop a simple tool capable of determining groups of individuals sharing common properties, whether sedimentological, diagenetic or petrophysical. Through LDA, it has been confirmed that depositional setting, diagenesis and petrophysical properties are linked, explaining why different sedimentary sub-facies clearly have different reservoir properties. This innovative methodology opens new perspectives to study cored *Oolithe Blanche Formation* strata at basin scale.

Today and in the future, carbonate reservoirs will continue to be a major issue for hydrocarbon exploitation, storage and geothermal energy. However, the distribution of their sedimentary and petrophysical heterogeneities still requires further investigation. Here, we have developed a high-resolution methodology, based on sedimentology, diagenesis and petrophysics, in a carbonate reservoir presenting subtle differences, with orders of variability that are not classically considered in reservoir modelling. We have shown that the petrophysical heterogeneities observed relate to specific sedimentological or diagenetic parameters and that these heterogeneities can therefore be predicted. With the vast quantities of data accumulated worldwide, it now becomes necessary to undertake more detailed investigations of carbonate reservoirs at a smaller scale, using microstructure to better understand macrostructure. Extensive studies, such as those presented here, defining the relationships between parameters and heterogeneities, improve and deepen global knowledge of carbonate reservoirs.

Acknowledgements

This work was partly funded by the CNRS INSU-CESUR project and was supported by the French Geological Survey (BRGM, Bureau

de Recherches Géologiques et Minières, Orléans, France). We would like to thank Jerry Lucia (University of Texas at Austin) and John Reijmer for their constructive comments on a previous version of the manuscript. Alex MacNeil, Veerle Vandeginste and an anonymous reviewer are also thanked for their constructive suggestions. We thank Carmela Chateau-Smith for proof-reading the English. This work could not have been carried out without the cooperation of Rocamat and more especially of Gilles Jouillero. We also wish to thank Youri Hamon, Marc de Rafelis, Alexandre Lethiers, Frédéric Delbès, Nathalie Labourdette, Jérôme Wasserman, Jean-Christian Colombier, and Lisa Texier for their support.

References

- Anselmetti, F.S., Eberli, G.P., 1993. Controls on sonic velocity in carbonates. *Pure Appl Geophys* 141, 287–323.
- Archie, G.E., 1942. The electrical resistivity log as an aid in determining some reservoir characteristics. *Trans. AIME* 146, 54–62.
- Baechle, G.T., Colpaert, A., Eberli, G.P., Weger, R.J., 2008. Effects of microporosity on sonic velocity in carbonate rocks. *Lead. Edge* 27, 1012–1018.
- Baechle, G.T., Weger, R.J., Eberli, G.P., Massafiero, J.L., Sun, Y.-F., 2005. Changes of shear moduli in carbonate rocks: implications for Gassmann applicability. *Lead. Edge* 24, 507–510.
- Beccaletto, L., Hanot, F., Serrano, O., Marc, S., 2010. Overview of the subsurface structural pattern of the Paris Basin (France): insights from the reprocessing and interpretation of regional seismic lines. *Mar. Pet. Geol.* 28, 861–879.
- Brigaud, B., Durllet, C., Deconinck, J.F., Vincent, B., Thierry, J., Trouiller, A., 2009. The origin and timing of multiphase cementation in carbonates: impact of regional scale geodynamic events on the Middle Jurassic Limestones diagenesis (Paris Basin, France). *Sediment. Geol.* 222, 161–180.
- Brigaud, B., Vincent, B., Durllet, C., Deconinck, J.F., Blanc, P., Trouiller, A., 2010. Acoustic properties of ancient shallow-marine carbonates: effects of depositional environments and diagenetic processes (Middle Jurassic, Paris Basin, France). *J. Sediment. Res.* 80, 791–807.
- Brosse, E., Badinier, G., Blanchard, F., Caspard, E., Collin, P.Y., Delmas, J., Dezayes, C., Dreux, R., Dufournet, A., Durst, P., Fillacier, S., Garcia, D., Grataloup, S., Hanot, F., Hasanov, V., Houel, P., Kervevan, C., Lansart, M., Lescanne, M., Menjoz, A., Monnet, M., Mougou, P., Nedelec, B., Poutrel, A., Rachez, X., Renoux, P., Rigollet, C., Ruffier-Meray, V., Saysses, S., Thion, I., Thoraval, A., Vidal-Gilbert, S., 2010. Selection and characterization of geological sites able to host a pilot-scale CO₂ storage in the Paris basin (GeoCarbone-PICOREF). *Oil Gas Sci. Technol.* 65, 375–403.
- Burchette, T.P., 2012. Carbonate Rocks and Petroleum Reservoirs: a Geological Perspective from the Industry. In: Geological Society, London, Special Publications 370, pp. 17–37.
- Casteleyn, L., Robion, P., Collin, P.Y., Menéndez, B., David, C., Desaubiaux, G., Fernandes, N., Dreux, R., Badinier, G., Brosse, E., Rigollet, C., 2010a. Interrelations of the petrophysical, sedimentological and microstructural properties of the *Oolithe Blanche Formation* (Bathonian, saline aquifer of the Paris Basin). *Sediment. Geol.* 230, 123–138.
- Casteleyn, L., Robion, P., David, C., Collin, P.Y., Menéndez, B., Fernandes, N., Desaubiaux, G., Rigollet, C., 2010b. An integrated study of the petrophysical properties of carbonate rocks from the *Oolithe Blanche formation* in the Paris Basin. *Tectonophysics* 503, 18–33.
- Cole, D.I., 1976. Velocity/porosity relationships in limestones from the Portland group of Southern England. *Geoprospection* 14, 37–50.
- Cornillon, P.-A., Matzner-Løber, E., 2007. Régression. Théorie et applications. Collection Statistique et Probabilités Appliquées. Springer, France.
- Croizé, D., Ehrenberg, S.N., Bjørlykke, K., Renard, F., Jahren, J., 2010. Petrophysical properties of bioclastic platform carbonates: implications for porosity controls during burial. *Mar. Pet. Geol.* 27, 1765–1774.
- Darcy, H., 1856. Les fontaines publiques de la ville de Dijon. Exposition et application des principes à suivre et des formules à employer dans les questions de distribution d'eau: ouvrage terminé par un appendice relatif aux fournitures d'eau de plusieurs villes au filtrage des eaux et à la fabrication des tuyaux de fonte, de plomb, de tôle et de bitume. Dalmont Ed.
- David, C., Menéndez, B., Mengus, J., 2011. X-ray imaging of water motion during capillary imbibition: geometry and kinetics of water front in intact and damaged porous rocks. *J. Geophys. Res.* 116, B03204.
- Davis, J.M., Roy, N.D., Mozley, P.S., Hall, J.S., 2006. The effect of carbonate cementation on permeability heterogeneity in fluvial aquifers: an outcrop analog study. *Sediment. Geol.* 184, 267–280.
- Delmas, J., Brosse, E., Houel, P., 2010. Petrophysical properties of the Middle Jurassic carbonates in the PICOREF Sector (South Champagne, Paris Basin, France). *Oil Gas Sci. Technol. – Rev. Inst. Fr. Pétrole* 65, 405–434.
- Dickson, J.A.D., 1966. Carbonate identification and genesis as revealed by staining. *J. Sediment. Res.* 36, 491–505.
- Dou, Q., Sun, Y., Sullivan, C., 2011. Rock-physics-based carbonate pore type characterization and reservoir permeability heterogeneity evaluation, Upper San Andres reservoir, Permian Basin, west Texas. *J. Appl. Geophys.* 74, 8–18.

- Dromart, G., Garcia, J.P., Gaumet, F., Picard, S., Rousseau, M., Atrops, F., Lecuyer, C., Sheppard, S.M.F., 2003. Perturbation of the carbon cycle at the Middle/Late Jurassic transition: geological and geochemical evidence. *Am. J. Sci.* 303, 667–707.
- Duguid, S.M.A., Kyser, T.K., James, N.P., Rankey, E.C., 2010. Microbes and ooids. *J. Sediment. Res.* 80, 236–251.
- Dvorkin, J., Mavko, G., Nur, A., 1991. The effect of cementation on the elastic properties of granular material. *Mech. Mat.* 12, 207–217.
- Dvorkin, J., Nur, A., Yin, H., 1994. Effective properties of cemented granular materials. *Mech. Mat.* 18, 351–366.
- Fabricius, I.L., Bächle, G.T., Eberli, G.P., 2010. Elastic moduli of dry and water-saturated carbonates—effect of depositional texture, porosity, and permeability. *Geophysics* 75, N65–N78.
- Floquet, M., Laurin, B., Laville, P., Marchand, D., Menot, J.C., Pascal, A., Thierry, J., 1989. Les systèmes sédimentaires bourguignons d'âge bathonien terminal-callovien. *Bull. Centres Rech. Explor. Prod. Elf-Aquitaine* 13, 133–165.
- Flügel, E., 2004. *Microfacies of Carbonate Rocks: Analysis, Interpretation and Application*. Springer Verlag.
- Fournier, F., Leonide, P., Biscarrat, K., Gallois, A., Borgomano, J., Foubert, A., 2011. Elastic properties of microporous cemented grainstones. *Geophysics* 76, E211–E226.
- Garcia, J.-P., Laurin, B., Sambet, G., 1996. Les associations de brachiopodes du Jurassique moyen du bassin de Paris: une échelle biochronologique ponctuée de niveaux repères pour la contrainte des corrélations séquentielles à haute résolution. *Bull. Soc. géol. Fr.* 167, 435–451.
- Gaumet, F., Garcia, J.-P., Dromart, G., Sambet, G., 1996. Contrôle stratigraphique des faciès, géométries et profils de dépôt de la plate-forme carbonatée bourguignonne au Bathonien-Callovien. *Bull. Soc. géol. Fr.* 167, 409–421.
- Glover, P., 2009. What is the cementation exponent? A new interpretation. *Lead. Edge* 28, 82–85.
- Graton, L.C., Fraser, H.J., 1935. Systematic packing of spheres: with particular relation to porosity and permeability. *J. Geol.*, 785–909.
- Guillocheau, F., Robin, C., Allemand, P., Bourquin, S., Brault, N., Dromart, G., Friedenber, R., Garcia, J.-P., Gaulier, J., Gaumet, F., 1999. Évolution géodynamique du bassin de Paris: apport d'une base de données stratigraphiques 3D. *Bull. Inf. Géol. Bass. Paris* 36, 3–35.
- Harris, P.M., 1979. Facies Anatomy and Diagenesis of a Bahamian Ooid Shoal. Comparative Sedimentology Laboratory, Division of Marine Geology and Geophysics, University of Miami, Rosenstiel School of Marine & Atmospheric Science.
- Harris, P.M., Halley, R.B., Lukas, K.J., 1979. Endolith microborings and their preservation in Holocene–Pleistocene (Bahama-Florida) ooids. *Geology* 7, 216–220.
- Lachenbruch, P.A., Goldstein, M., 1979. Discriminant analysis. *Biometrics*, 69–85.
- Lindholm, R.C., Finkelman, R.B., 1972. Calcite staining; semiquantitative determination of ferrous iron. *J. Sediment. Res.* 42, 239–242.
- Lion, M., Skoczylas, F., Ledesert, B., 2004. Determination of the main hydraulic and poro-elastic properties of a limestone from Bourgogne, France. *Int. J. Rock Mech. Min. Sci.* 41, 915–925.
- Lønøy, A., 2006. Making sense of carbonate pore systems. *AAPG Bull.* 90, 1381–1405.
- Lucia, F.J., 2007. *Carbonate Reservoir Characterization: an Integrated Approach*, second ed. Springer.
- Mégnién, C., 1979. Hydrogéologie du centre du bassin de Paris: contribution à l'étude de quelques aquifères principaux. Éditions du B.R.G.M.
- Pacton, M., Ariztegui, D., Wacey, D., Kilburn, M.R., Rollion-Bard, C., Farah, R., Vasconcelos, C., 2012. Going nano: a new step toward understanding the processes governing freshwater ooid formation. *Geology* 40, 547–550.
- Palermo, D., Aigner, T., Nardon, S., Blendinger, W., 2010. Three-dimensional facies modeling of carbonate sand bodies: outcrop analog study in an epicontinental basin (Triassic, southwest Germany). *AAPG Bull.* 94, 475–512.
- Pomerol, C., 1978. Evolution paléogéographique et structurale du Bassin de Paris, du Précambrien à l'Actuel, en relation avec les régions avoisinantes. *Geol. Mijnb.* 57, 533–543.
- Purser, B.H., 1983. Sédimentation et diagenèse des carbonates néritiques récents: Les éléments de la sédimentation et de la diagenèse. Editions Technip.
- Qi, L., Carr, T.R., Goldstein, R.H., 2007. Geostatistical three-dimensional modeling of oolite shoals, St. Louis Limestone, southwest Kansas. *Aapg Bull.* 91, 69–96.
- Rankey, E.C., Reeder, S.L., 2010. Controls on platform-scale patterns of surface sediments, shallow Holocene platforms, Bahamas. *Sedimentology* 57, 1545–1565.
- Rankey, E.C., Reeder, S.L., 2011. Holocene oolitic marine sand complexes of the Bahamas. *J. Sediment. Res.* 81, 97–117.
- Reeder, S.L., Rankey, E.C., 2008. Interactions between tidal flows and ooid shoals, northern Bahamas. *J. Sediment. Res.* 78, 175–186.
- Reeder, S.L., Rankey, E.C., 2009. Controls on morphology and sedimentology of carbonate tidal deltas, Abacos, Bahamas. *Mar. Geol.* 267, 141–155.
- Reijmer, J.J.G., Swart, P.K., Bauch, T., Otto, R., Reuning, L., Roth, S., Zechel, S., 2009. A Re-Evaluation of Facies on Great Bahama Bank I: New Facies Maps of Western Great Bahama Bank. In: *Perspectives in Carbonate Geology: a Tribute to the Career of Robert Nathan Ginsburg*, 98, pp. 29–46 (Special Publication 41 of the IAS).
- Rezaee, M.-R., Motiei, H., Kazemzadeh, E., 2007. A new method to acquire m exponent and tortuosity factor for microscopically heterogeneous carbonates. *J. Pet. Sci. Eng.* 56, 241–251.
- Riepe, L., Sachs, W., Schopper, J., 1983. Pressure Effects on Permeability, Transitions, Eight European Formation Evaluation Symposium. London Soc. of Prof. Well Log Analysts, London, England, p. 15. March.
- Rong, H., Jiao, Y., Wu, L., Gu, Y., Zhang, L., Li, R., Zeng, F., 2012. Effects of diagenesis on the acoustic velocity of the Triassic oolitic shoals in the Yudongzi outcrop of Erlangmiao area, Northwest Sichuan Basin. *J. Earth Sci.* 23, 542–558.
- Sandberg, P.A., 1983. An oscillating trend in phanerozoic non-skeletal carbonate mineralogy. *Nature* 305, 19–22.
- Schlumberger, 2007. Schlumberger Market Analysis, 2007. Schlumberger, p. 14.
- Shapiro, S.S., Wilk, M.B., 1965. An analysis of variance test for normality (complete samples). *Biometrika* 52, 591–611.
- Shearman, D., Twyman, J., Zand Karimi, M., 1970. The genesis and diagenesis of oolites. *Proc. Geol. Assoc.* 81, 561–564.
- Team, R.C., 2012. R: a Language and Environment for Statistical Computing. R Foundation for Statistical Computing, Vienna, Austria.
- Tiab, D., Donaldson, E.C., 2012. *Petrophysics – Theory and Practice of Measuring Reservoir Rock and Fluid Transport Properties*, third ed. Elsevier, p. 976.
- Tucker, M.E., Wright, V.P., Dickson, J.A.D., 1990. *Carbonate Sedimentology*. Wiley-Blackwell.
- Van Brakel, J., Modry, S., Svata, M., 1981. Mercury porosimetry: state of the art. *Powder Technol.* 29, 1–12.
- Van Geet, M., Lagrou, D., Swennen, R., 2003. Porosity Measurements of Sedimentary Rocks by Means of Microfocus X-ray Computed Tomography (μ CT). In: *Geological Society, London, Special Publications* 215, pp. 51–60.
- Verwer, K., Braaksma, H., Kenter, J.A., 2008. Acoustic properties of carbonates: effects of rock texture and implications for fluid substitution. *Geophysics* 73, B51–B65.
- Verwer, K., Eberli, G.P., Weger, R.J., 2011. Effect of pore structure on electrical resistivity in carbonates. *AAPG Bull.* 95, 175–190.
- Verwer, K., Porta, G.D., Merino-Tomé, O., Kenter, J.A.M., 2009. Controls and predictability of carbonate facies architecture in a Lower Jurassic three-dimensional barrier-shoal complex (Djebel Bou Dahar, High Atlas, Morocco). *Sedimentology* 56, 1801–1831.
- Vincent, B., Fleury, M., Santerre, Y., Brigaud, B., 2011. NMR relaxation of neritic carbonates: an integrated petrophysical and petrographical approach. *J. Appl. Geophys.* 74, 38–58.
- Washburn, E.W., 1921. Note on a method of determining the distribution of pore sizes in a porous material. *Proc. Natl. Acad. Sci. U. S. A.* 7, 115–116.
- Weger, R.J., Eberli, G.P., Baechle, G.T., Massafiero, J.L., Sun, Y.-F., 2009. Quantification of pore structure and its effect on sonic velocity and permeability in carbonates. *AAPG Bull.* 93, 1297–1317.
- Westphal, H., Eberli, G.P., Smith, L.B., Grammer, G.M., Kislak, J., 2004. Reservoir characterization of the Mississippian Madison Formation, Wind River basin, Wyoming. *AAPG Bull.* 88, 405–432.
- Wilson, M.E.J., Evans, M.J., 2002. Sedimentology and diagenesis of Tertiary carbonates on the Mangkalihit Peninsula, Borneo: implications for subsurface reservoir quality. *Mar. Pet. Geol.* 19, 873–900.
- Wold, S., Esbensen, K., Geladi, P., 1987. Principal component analysis. *Chemom. Intell. Lab. Syst.* 2, 37–52.
- Worthington, P.F., 1993. The uses and abuses of the Archie equations, 1: the formation factor-porosity relationship. *J. Appl. Geophys.* 30, 215–228.
- Zinsner, B., Pellerin, F.M., 2007. *A Geoscientist's Guide to Petrophysics*. Editions Technip.